
Article:
Chaves, V., Navarro, A., Susmel, L. orcid.org/0000-0001-7753-9176 et al. (1 more author) (2022) Analysis of biaxial fatigue limit models for cases with circular notches. International Journal of Fatigue, 162. 106981. ISSN 0142-1123

https://doi.org/10.1016/j.ijfatigue.2022.106981

International Journal of Fatigue 162 (2022) 106981

Contents lists available at ScienceDirect

International Journal of Fatigue

journal homepage: www.elsevier.com/locate/ijfatigue

Analysis of biaxial fatigue limit models for cases with circular notches

V. Chaves [a,*], A. Navarro [a], L. Susmel [b], D. Taylor [c]

[a] Departamento de Ingeniería Mecánica y Fabricación, Escuela Técnica Superior de Ingeniería, Universidad de Sevilla, Camino de los Descubrimientos s/n, 41092 Sevilla, Spain
[b] Department of Civil and Structural Engineering, The University of Sheffield, Mappin Street, Sheffield S1 3JD, United Kingdom
[c] Department of Mechanical Engineering, Trinity College, Dublin 2, Ireland

ARTICLE INFO

Keywords:
Multiaxial fatigue
Notch
High cycle fatigue
Fatigue limit
Biaxial cyclic loading

ABSTRACT

This work shows an analysis of several models of multiaxial fatigue for notches: Navarro-Rios' model, which analyses the interaction between the crack and its associated plastic zone with the material microstructural barriers, and three models that combine a critical volume method for notches with a critical plane model for multiaxial fatigue in unnotched solids. Specifically, the application of these models for the prediction of the fatigue limit for a plate with a circular hole subjected to axial, shear and in-phase biaxial cyclic loading is studied. The effects of two parameters are analysed: the radius of the hole and the relationship between the torsional and axial fatigue limits. For all the analysed models, cases are observed in which an increase in the hole radius produces an increase in the predicted fatigue limit, that is, the evolution of the fatigue limit with an increasing hole radius is not always monotonically decreasing, as would be expected. These effects, which we have called "humps" because of their appearance on the prediction graphs, mainly occur in shear loading. No humps were observed in the studied experimental results, but the number of available experimental results is too small to assure this tendency. The results shown in the work indicate that a greater knowledge of the physics of multiaxial fatigue in notches is necessary to achieve models that are capable of providing increasingly accurate predictions.

1. Introduction

It is well known that fatigue failure occurs very frequently from stress concentrations or notches. Various models for predicting fatigue failure in the presence of notches have been published since the 1950s, with the so-called critical volume models being probably most widely used. These models include the classic Neuber [1] and Peterson models [2], and, more recently, the Theory of Critical Distances (TCD) [3]. They are based on assessing the stress in a certain volume of material ahead of the notch root. Fatigue failure occurs if the average stress in this volume reaches a certain critical value. The size of the critical volume is material dependent. Within the Critical Distance Methods of Taylor, the point method (PM) stands out for its simplicity and good predictions. In the PM, fatigue failure is predicted from the elastic stress at a single point, located at a distance $L/2$ from the notch edge, where L is El Haddad's short crack parameter of the material. Failure will occur if the maximum principal stress at the distance $L/2$ equals the material endurance limit or fatigue limit. From a different point of view, some short-crack growth models, such as Navarro-Rios' model, have been developed to predict fatigue failure at notches [4,5,6]. Navarro-Rios' model analyses the capability of the crack, which is formed at the notch root, and its associated plastic zone, to overcome successive microstructural barriers such as grain boundaries. It is assumed that the plastic displacement takes place in rectilinear slip bands across grains in the solid. The microcrack nucleates in the most favourable grain and within this grain the plastic zone spreads from the crack tip to the grain boundary, where it is arrested. The crack, the plastic zone and the barrier are modelled by means of a continuous distribution of dislocations. This allows a correct representation of these three zones and the obtaining of the local stress at the barrier as a function of the applied stress. If the applied stress is high enough, plastic slip will be promoted into the next grain. Crack propagation and blocking at the grain boundary would occur in each successive grain. Fatigue failure occurs if the crack spreads through the successive grains.

All the presented models were developed to study cases of axial cyclic loading. However, components are frequently subject to multiaxial cyclic loading. The study of plain specimens under multiaxial cyclic loading has received the attention of many researchers for quite some time, and several failure prediction models have been proposed, including the so-called "critical plane" models, such as the model of

* Corresponding author.
E-mail address: chavesrv@us.es (V. Chaves).

https://doi.org/10.1016/j.ijfatigue.2022.106981
Received 18 March 2022; Received in revised form 29 April 2022; Accepted 2 May 2022
Available online 11 May 2022

Findley [7] and the model of Brown and Miller [8]. These models are based on the evidence that the fatigue crack grows on a certain plane and correlate fatigue failure with reaching a certain value of stresses or strains in the critical plane. Despite the long time devoted by the scientific community to the prediction of failure in multiaxial fatigue, the results provided by the most widespread models are very different from one another even for relatively simple cases such as the case of a proportional biaxial stress [9], which indicates that it is necessary to continue improving the multiaxial fatigue models.

The combination of the presence of a notch and the application of multiaxial cyclic loading implies a problem of even greater complexity. Experimental studies in this combined field are not so extensive and existing models are not so consolidated. Focusing on high-cycle fatigue, in the experimental field, the extensive classical work of Gough et al. in specimens containing complex stress raisers made of various materials and subjected to in-phase bending-torsion loading is remarkable [10]. More recently, Endo and Murakami tested cylindrical specimens with small superficial circular holes under bending and torsion [11], Susmel and Taylor tested notched cylindrical samples under in- and out-of-phase biaxial situations, including non-zero mean values and different frequencies [12], and plates with an inclined V-notch subject to in-phase mixed Mode I/II loadings [13]. Fatemi et al. [14] and Chaves et al. [15,16] tested cylindrical specimens with a circular hole under biaxial loading. Regarding the models in this field, most are relatively recent. Proposals that combine a critical volume model for notches with a critical plane model for multiaxial fatigue stand out, such as the combined model proposed by Taylor and Susmel [17]. With a different philosophy, there is a version for notched solids under multiaxial loading of Navarro-Rios' short-crack model [18].

Comparing the predictions obtained with various notch multiaxial fatigue models for simple geometry and load cases can provide great insight into the degree of accuracy and reliability of the model predictions. This information can be supplemented by comparing some of these model predictions with some experimental cases. As for smooth specimens, this type of study can help to determine the current models' degree of maturity for notches in multiaxial fatigue and if an evolution, or certain modifications, are necessary to obtain more accurate predictions. It could also indicate the need for a specific test campaign to verify whether or not certain trends in the model predictions are correct.

This paper shows an analysis of various multiaxial fatigue models for notches. The study is focused on high cycle fatigue and the study of the endurance limit, or the fatigue limit, for axial, torsional and in-phase biaxial cyclic loading in specimens with a circular notch. The analysis is conducted based on two parameters: the radius of the circular hole R and the ratio between the torsional and axial endurance limits, or fatigue limits, τ_{FL}/σ_{FL}, which is an indicator of the ductile or brittle behaviour of the material in fatigue (for simplicity, only the term "fatigue limit" will be used from now on). Finally, a comparison between the experimental results from the literature and predictions with the models is presented.

2. Description of the models

In this section a brief description of several models of multiaxial notch fatigue is presented. The models are as follows: the model resulting from the combination of Taylor's Theory of Critical Distances and Susmel's Critical Plane Method (TCD + MWCM) [17], the multiaxial critical plane criterion combined with the PM proposed by Carpinteri et al. [19] and the microstructural model of Navarro and de los Rios for biaxial loading in notches (Biaxial N-R model) [18].

2.1. The combined model of Taylor and Susmel (TCD + MWCM)

Taylor and Susmel proposed using a combination of one of Taylor's methods of critical distance for notches under axial loading (TCD) with the critical plane method proposed by Susmel for multiaxial fatigue in unnotched components, the Modified Whöler Curve Method (MWCM) [3,17], to study the effect of notches under multiaxial fatigue loading. If the PM is chosen as the critical distance method, then the combined method for calculating the fatigue limit in a notched component consists of locating the point of maximum stress at the edge of the notch (the *hot-spot*) and determining the critical plane at a point located at a distance of $L/2$, where L is the critical distance of the material for TCD and is defined as $L = (1/\pi)(\Delta K_{th}/\Delta\sigma_{FL})^2$, where ΔK_{th} is the threshold value of ΔK for fatigue crack growth and $\Delta\sigma_{FL}$ is the fatigue limit range of the material, at $R_\sigma = -1$. Then, L is equal to the material length a_0 used by El Haddad et al. [20]. The direction along which this distance is measured gives rise to two variants discussed below. The critical plane is chosen as that plane passing through the point located at $L/2$ from the hot-spot which has the largest value of the amplitude of the shear stress τ_a. The stress normal to this critical plane is denoted as $\sigma_{n,max}$. Once both stresses are known, the fatigue limit is reached if the following criterion is met:

$$\tau_a + \left(\tau_{FL} - \frac{\sigma_{FL}}{2}\right)\frac{\sigma_{n,max}}{\tau_a} = \tau_{FL} \tag{1}$$

Where τ_{FL} is the torsional fatigue limit. There are two variants of the method, depending on where the point at $L/2$ is located, which we will call Mode I variant and Mode II variant.

Mode I variant

In the Mode I variant, the point at a distance *L/2* from the hot-spot is located on a straight line emanating from the assumed crack initiation location and perpendicular to the component surface at the hot spot itself [21,17]. The direction of the line can be considered as the direction corresponding to a crack formed by normal stresses, i.e. growing in Mode I. A scheme of the crack line for this variant for a plate with a

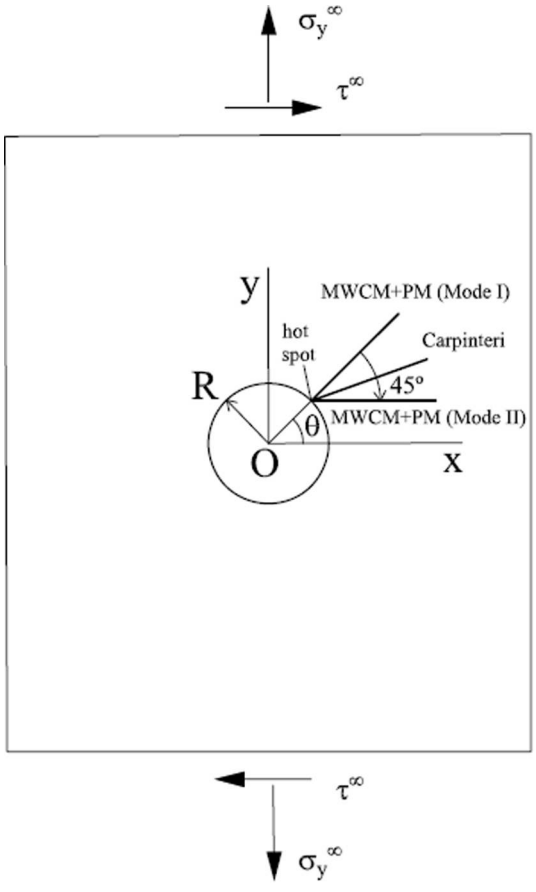

Fig. 1. Crack lines for the MWCM + PM and Carpinteri et al. models.

circular notch subjected to biaxial loading, σ_y^∞ and τ^∞, is shown in Fig. 1. It is worth remembering here also that the focus path is suggested as being taken coincident with the notch bisector when stress concentrators are modelled by imposing that the notch root radius equals zero [17].

Mode II variant

In the Mode II variant, the point at a distance $L/2$ from the hot-spot is on a line forming 45° to the line normal to the notch surface at the hot-spot; that is, in the direction of the maximum shear stress at the hot-spot [22,3]. This would be the direction corresponding to a crack formed by shear stresses; that is, a crack growing in Mode II (see Fig. 1).

2.2. The combined model of Carpinteri et al.

This model is qualitatively similar to the previous one, since it is based on extending a multiaxial fatigue critical plane model to the case of notches by incorporating a critical distance method, specifically the PM [19]. As in the previous model, the stresses are analysed at a point located at $L/2$ from the maximum stress point or hot spot, which is considered the crack initiation point. The direction of the line where the point is located depends on the material and is defined by the angle δ with respect to the line normal to the surface at the hot spot:

$$\delta = \frac{3\pi}{8}\left[1 - \left(\frac{\tau_{FL}}{\sigma_{FL}}\right)^2\right] \tag{2}$$

The crack line for this model lies between the crack lines for the two MWCM + PM variants, as sketched in Fig. 1. For a material completely brittle in fatigue, with $\tau_{FL}/\sigma_{FL} = 1$, the value of δ is 0; therefore, the line chosen is that of the Mode I variant, while for a material with $\tau_{FL}/\sigma_{FL} = 1/\sqrt{3}$ the line is at 45°, i.e. Mode II variant. For intermediate values of the relation τ_{FL}/σ_{FL} intermediate directions are also obtained. Once the direction of the crack line and the position of the point are defined, the maximum normal stress N_{max} and the shear stress C in the critical plane at the critical point are evaluated, with the normal to the critical plane defined as the line perpendicular to the crack line. An equivalent stress and the fatigue limit criterion are defined by the following equation:

$$\sigma_{eq,a} = \sqrt{N_{max}^2 + \left(\frac{\sigma_{FL}}{\tau_{FL}}\right)^2 C_a^2} = \sigma_{FL} \tag{3}$$

Please note that a different notation for normal and shear stress has been used in Eqs. (1) and (3). This has been done to facilitate as much as possible the comparisons with the original works.

2.3. Biaxial Navarro-Rios' model (biaxial N-R model)

The Navarro and de los Rios microstructural model (N-R model) [4,5] studies the interaction of the crack and its associated plastic zone with microstructural barriers, such as grain boundaries. The authors modelled the crack as a straight line. Mathematically, the crack, its associated plastic zone and the microstructural barrier are modelled by a distribution of dislocations. The remote stress required for the crack to overcome each successive barrier is then calculated. The maximum of that succession of calculated remote stresses will be the fatigue limit of the component. According to [23], this maximum value corresponds to the first local maximum. The model has been applied to predict the fatigue limit of notched components subject to fatigue axial loading [6,23]. The model has also been extended to in-phase biaxial loading [24]. For the case of a notched component under in-phase biaxial loading, two sets of dislocations are employed to account for the climb and glide components of displacements. The conditions for activation of dislocations sources in the neighbouring grain are established and this leads to a biaxial criterion, which is as follows (for a detailed description see [18]):

$$\frac{\sigma_3^i}{m_{\sigma i}^* \cdot \tau_c} + \frac{\tau_3^i}{m_{\tau i}^* \cdot \tau_c} = 1 \tag{4}$$

The parameters σ_3^i and τ_3^i represent the stresses at the i-th barrier, obtained from the equilibrium of dislocations in the crack line for the specific geometry and applied loads. This equilibrium involves the forces between dislocations, which depend on the geometry of the notch, and the normal and shear linear elastic stresses at the crack line, obtained from an analysis of the un-cracked solid, as in the Bueckner's superposition technique. Mathematically it gives rise to singular integral equations, which are transformed into a system of algebraic equations by means of quadratures. The parameters $m_{\sigma i}^*$ and $m_{\tau i}^*$ are orientation factors that project the stresses at the i-th barrier onto the sliding plane and the sliding direction of the source of dislocations, and τ_c is the critical stress needed to activate the dislocation sources in the (i + 1)-th grain. Their values are adjusted for the specific material from its axial and torsional fatigue limits, τ_{FL} and σ_{FL}, respectively, from the average grain size d and from the Kitagawa-Takahashi diagram of the plain material. The values of $m_{\sigma 1}^* \cdot \tau_c$ and $m_{\tau 1}^* \cdot \tau_c$, which are the constants of the criterion for the first grain, are as follows (the values for the following grains are based on the values for the first grain and the Kitagawa-Takahashi diagram):

$$m_{\sigma 1}^* \cdot \tau_c = \frac{\pi}{2 \cdot \cos^{-1} n} \bullet \frac{\sigma_{FL}}{\left(2 - \frac{\sigma_{FL}}{\tau_{FL}}\right)} \tag{5}$$

$$m_{\tau 1}^* \cdot \tau_c = \frac{\pi}{2 \cdot \cos^{-1} n} \bullet \frac{\sigma_{FL}}{\sqrt{\frac{\sigma_{FL}}{\tau_{FL}} - 1}} \tag{6}$$

where n is the ratio between the crack length and the crack + barrier length. For a plate with a circular notch subjected to in-phase biaxial cyclic loading, σ_y^∞ and τ^∞, the calculation of the biaxial loading necessary to overcome the successive barriers along the crack line is repeated for all possible directions, defined by the crack initiation point (angle θ) and the angle of the direction of the crack (angle θ_1) (see Fig. 2). The direction for which overcoming successive barriers requires the least remote biaxial applied stress will provide the sought biaxial fatigue limit. In this direction, the barrier that requires the highest applied stress to be overcome will be the so-called "decisive barrier", which defines the value of the notch fatigue limit.

3. Predictions using the models

Fatigue limit predictions in the case of an infinite plate with a circular hole subject to in-phase biaxial cyclic loading were made with the previously presented models. The material properties of a specific stainless steel (AISI 304L) tested in our laboratory were used for the predictions with the models in the parametric study of this section: average grain size $d = 0.08$ mm, El Haddad length $a_0 = L = 0.18$ mm, and axial fatigue limit $\sigma_{FL} = 316$ MPa ($R_\sigma = -1$) [15]. For calculating the linear elastic stresses in the torsional and axial fatigue limits, the analytical expression of Kirsch, available in elasticity books [25], was used. For the radius R, a wide range of values, from very small to very large, was studied. To analyze the influence of the parameter τ_{FL}/σ_{FL} in the models' predictions, virtual materials with the properties stated above and ratios of τ_{FL}/σ_{FL} that varied between 0.58 and 1 were studied. Specifically, three values were considered: $1/\sqrt{3} \cong 0.58$ (von Mises-type material), 0.75 and 1, which allowed us to analyse behaviour ranging from a ductile material in fatigue ($\tau_{FL}/\sigma_{FL} = 0.58$) to a brittle behaviour in fatigue ($\tau_{FL}/\sigma_{FL} = 1$), as well as an intermediate value. Predictions of the fatigue limit of the notched component σ_{FL}^N were obtained. For the biaxial N-R model, the number of algebraic equations was set to 200, the maximum crack length studied was set at 30 grains in length and the step of the θ and θ_1 angles for the study of the various

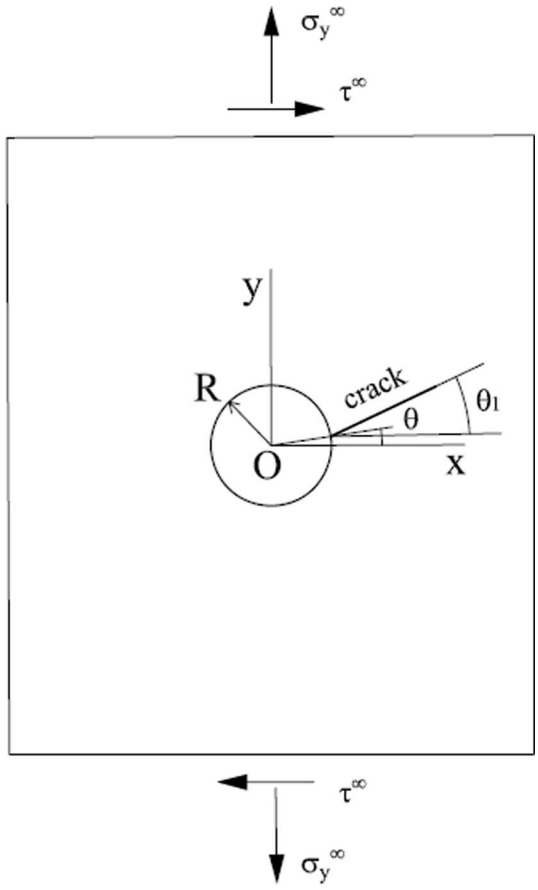

Fig. 2. Scheme of the crack initiation point and crack direction for the biaxial N-R model.

directions was set at 1°, all with the aim of achieving a high precision in the numerical solution without an excessive computational cost. The Kitawaga-Takahashi diagram was approximated with the equation proposed in [26], using f = 2.5. For the models of Taylor and Susmel, and Carpinteri et al., plane strain was assumed.

Three load cases were studied: pure axial, pure torsional and in-phase axial–torsional ($\sigma_y^\infty = \tau^\infty$), all of them fully reversed. The hot-spot for the three cases was located at the maximum principal stress points, i.e., $\theta = 0°$, $\theta = 45°$ and $\theta = 32°$, respectively. The positions of the hot-spots agree with the crack initiation points observed experimentally for this type of notched specimen and loading [15,16].

The predictions obtained with the different models for axial cyclic loading are shown in Fig. 3. Model predictions converge to approximately σ_{FL} for very small radii and to $\sigma_{FL}/K_t = \sigma_{FL}/3$ for large radii, which are the expected results. However, for intermediate radii the differences between the model predictions are quite noticeable, which is surprising for a case as simple as that of pure axial loading. The "type" of material, as per the τ_{FL}/σ_{FL} ratio, has an important influence, especially in the MWCM + PM model (Mode I variant), where the differences in the material-dependent predictions are quite large for R/a_0 values of approximately 1 (Fig. 3(a)). For the MWCM + PM model (Mode I variant) and brittle material in fatigue ($\tau_{FL}/\sigma_{FL} = 1$), it is observed that the curve is not monotonically decreasing, but that there is a small upward zone near $R/a_0 = 2$.

This material influence result contrasts with the predictions that would be obtained with an axial fatigue notch model, such as Taylor's PM [3] or the axial N-R model [6], which would give a single curve regardless of the value of the torsional fatigue limit τ_{FL}. Fig. 4 shows the predictions of the four models for a material with von Mises-type fatigue behaviour ($\tau_{FL}/\sigma_{FL} = 0.58$) which is a representative behaviour of ductile materials such as carbon steels, subjected to axial cyclic loading. Predictions with the PM and monoaxial N-R model have been added. There are considerable differences between the methods, especially in the vicinity of $R/a_0 = 0.3$, with differences greater than 20%.

The predictions of the four biaxial models for shear loading are shown in Fig. 5. For radii tending to zero, the model predictions approximately converge to the torsional fatigue limit, which is correct. For radii tending to infinity, the models approximately converge to $\tau_{FL}^N = \sigma_{FL}/K_t = \sigma_{FL}/4$, which is the expected result. It can be seen again that not all curves are monotonically decreasing, but that some of them have a rising and falling area, which we have called *humps*. These humps are particularly noticeable in the MWCM + PM model (Mode I). Furthermore, for the MWCM + PM model (Mode I) and a material with $\tau_{FL}/\sigma_{FL} = 1$, the curve shows values above 1 (for the case of $R/a_0 = 0.28$, it is predicted that $\tau_{FL}^N/\sigma_{FL} = 1.06$), that is, the fatigue limit of the notched component τ_{FL}^N is predicted to be above the fatigue limit of the plain component σ_{FL}, which is quite an unexpected result.

Fig. 6 shows the predictions of the four biaxial models for cyclic shear loading for a material with von Mises-type behaviour ($\tau_{FL}/\sigma_{FL} = 0.58$). The biaxial N-R and MWCM + PM (mode II) models give fairly close predictions, while the MWCM + PM (mode I) model shows more distant predictions. The differences between the model's predictions are greater than 20% in the vicinity of $R/a_0 = 0.5$. Furthermore, for all four models, the so-called humps are observed near $R/a_0 = 0.5$, the largest being that of the MWCM + PM model (Mode I).

For in-phase cyclic biaxial loading, the predictions of the models present an intermediate trend with respect to those shown previously for axial loading and shear loading. Fig. 7 shows the predictions of each of the four models for a biaxial in-phase load of the type $\sigma_y^\infty = \tau^\infty$. For radii tending to infinity, the models converge to approximately $\sigma_{FL}/K_t = \sigma_{FL}/5.47 = 0.18$, as expected, while for radii tending to zero the models give slightly more varied predictions, due to the different influences of the shear and normal stresses in each of the four fatigue limit criteria. The humps are clearly smaller than those in the case of shear loading, and, as shown in Fig. 8 for a von Mises material, the differences between the predictions of the four models are also smaller than in the case of shear loading.

4. Analysis of the humps by an elastic stress study near a circular hole

In some of the graphs in the previous section, primarily in the shear cases (Fig. 5), it has been shown that the evolution of the notched fatigue limit prediction curves is not monotonically decreasing, but has a rising and falling area that we call a hump. The reason for the existence of these humps may be related to the evolution along the crack line of some of the elastic stresses used in the criteria, which also present rises and falls. The effect of the elastic stresses evolution on the fatigue predictions evolution with the root radius for each of the four models is analysed next.

4.1. Elastic stress analysis for the MWCM + PM (Mode I) model

Fig. 9 shows the evolution of the elastic stresses in the line $\theta = \theta_1 = 45°$ as a function of the distance r to the centre of the hole divided by the hole radius R for an infinite plate with a circular hole subject to a remote applied stress of $\tau^\infty = -1$ MPa, i.e. shear loading. This line is the crack path used for predictions with the MWCM + PM (mode I variant) model for this type of applied load. Note that with the stress sign criterion adopted in this research, it is required to apply a stress $\tau^\infty = -1$ MPa to have the hot spot and the focus path in the first quadrant. It can be seen that the stress $\sigma_{\theta\theta}$ starts from a value of 4 MPa and monotonically decreases to a value of 1 MPa at far distances. The shear stress $\tau_{r\theta}$ is 0 for any distance r. The stress σ_{rr} starts from a value of 0 MPa to meet the boundary condition in the hole contour, rises to a maximum value of

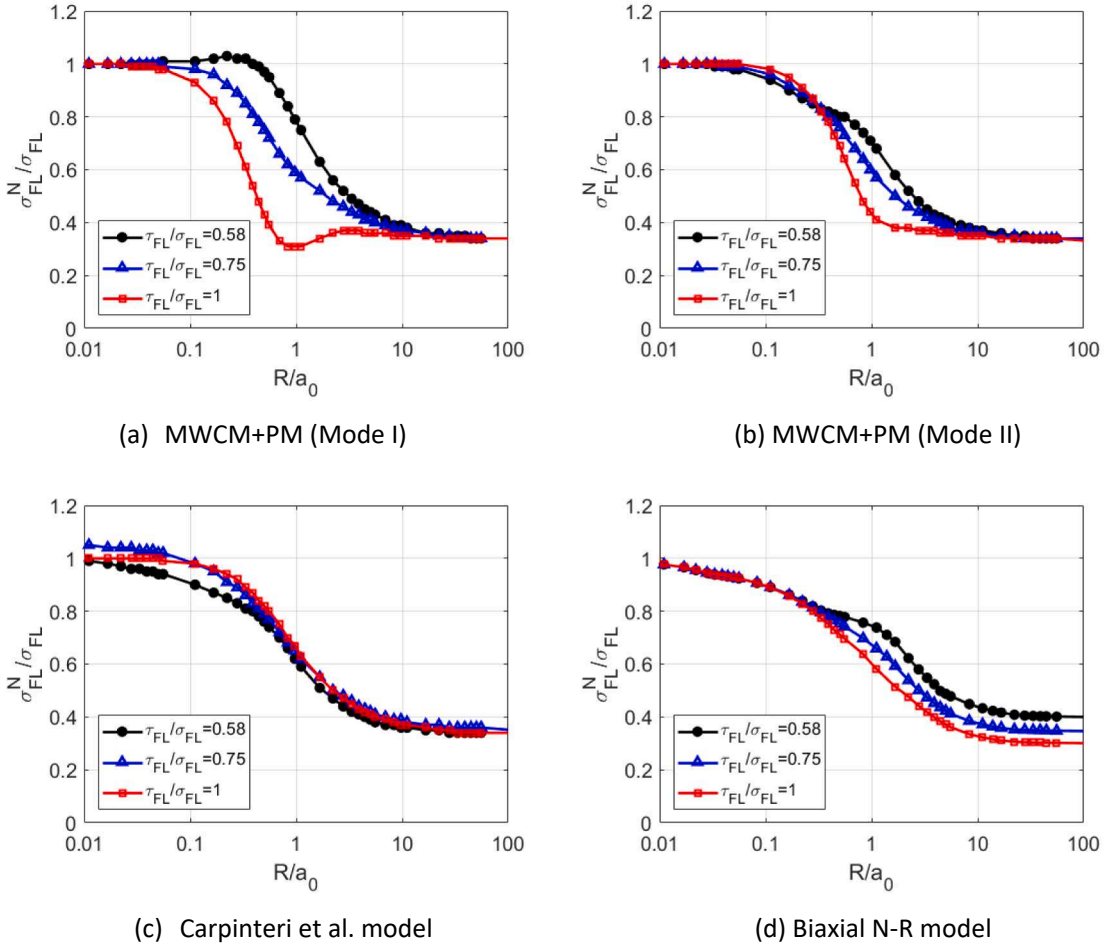

Fig. 3. Fatigue limit predictions for an infinite plate with a circular hole subjected to axial cyclic loading with several models: (a) MWCM + PM (Mode I) model, (b) MWCM + PM (Mode II) model, (c) Carpinteri et al. model and (d) Biaxial N-R model.

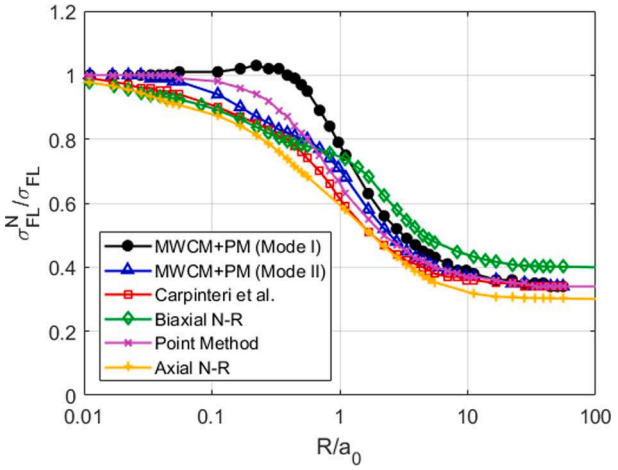

Fig. 4. Fatigue limit predictions of various models for a material with τ_{FL}/σ_{FL} = 0.58 for an infinite plate with a circular hole subjected to axial cyclic loading.

0.33 for $r/R = 1.22$, and then decreases to a value of −1 away from the hole. For this particular case, since the shear stress $\tau_{r\theta}$ is zero, the two stresses $\sigma_{\theta\theta}$ and σ_{rr} are principal stresses. For plane strain, the third principal stress is $\sigma_{zz} = \nu(\sigma_{\theta\theta} + \sigma_{rr})$, which has an intermediate evolution between the other two principal stresses for a considered value of υ = 0.3, as shown in Fig. 9. Therefore, the stresses $\sigma_{\theta\theta}$ and σ_{rr} are the principal stresses I and III, respectively.

The particular case of the prediction with the MWCM + PM model (Mode I variant) for a material with$\tau_{FL}/\sigma_{FL} = 0.5$ subjected to cyclic shear loading will now be studied, a case that allows a relatively simple analytical study. In the case $\tau_{FL}/\sigma_{FL} = 0.5$, the fatigue limit criterion, defined with Eq. (1), is greatly simplified, since $\tau_{FL} - \sigma_{FL}/2 = 0$, leaving the following expression:

$$\tau_a = \tau_{FL} \tag{7}$$

Therefore, in this particular case, the stress $\sigma_{n,max}$ is not used in the criterion, only the maximum shear stress τ_a, and the criterion is fulfilled when the stress τ_a reaches the value of the torsional fatigue limit τ_{FL}. As seen previously, since the stresses $\sigma_{\theta\theta}$ and σ_{rr} are the principal stresses I and III respectively, the maximum shear stress τ_a is:

$$\tau_a = \frac{\sigma_{\theta\theta} - \sigma_{rr}}{2} \tag{8}$$

The analytical expression for the shear stress τ_a, for $\theta = \theta_1 = 45°$, is taken directly from the expressions for $\sigma_{\theta\theta}$ and σ_{rr} for the shear case [27]:

$$\tau_a = \frac{\sigma_{\theta\theta} - \sigma_{rr}}{2} = -\frac{\tau^{\infty}}{2}\left(2 + 6\frac{R^4}{r^4} - 4\frac{R^2}{r^2}\right) \tag{9}$$

Fig. 9 shows its evolution (for $\tau^{\infty} = -1$ MPa) as a function of r/R. It is not monotonically decreasing. Instead, it has an initial downward part and a later upward part. It begins with a value of 2 for $r/R = 1$, continues downward, reaches a minimum, and then continues upward, tending to 1 as r/R tends to infinity. This non-monotonic evolution of τ_a clearly

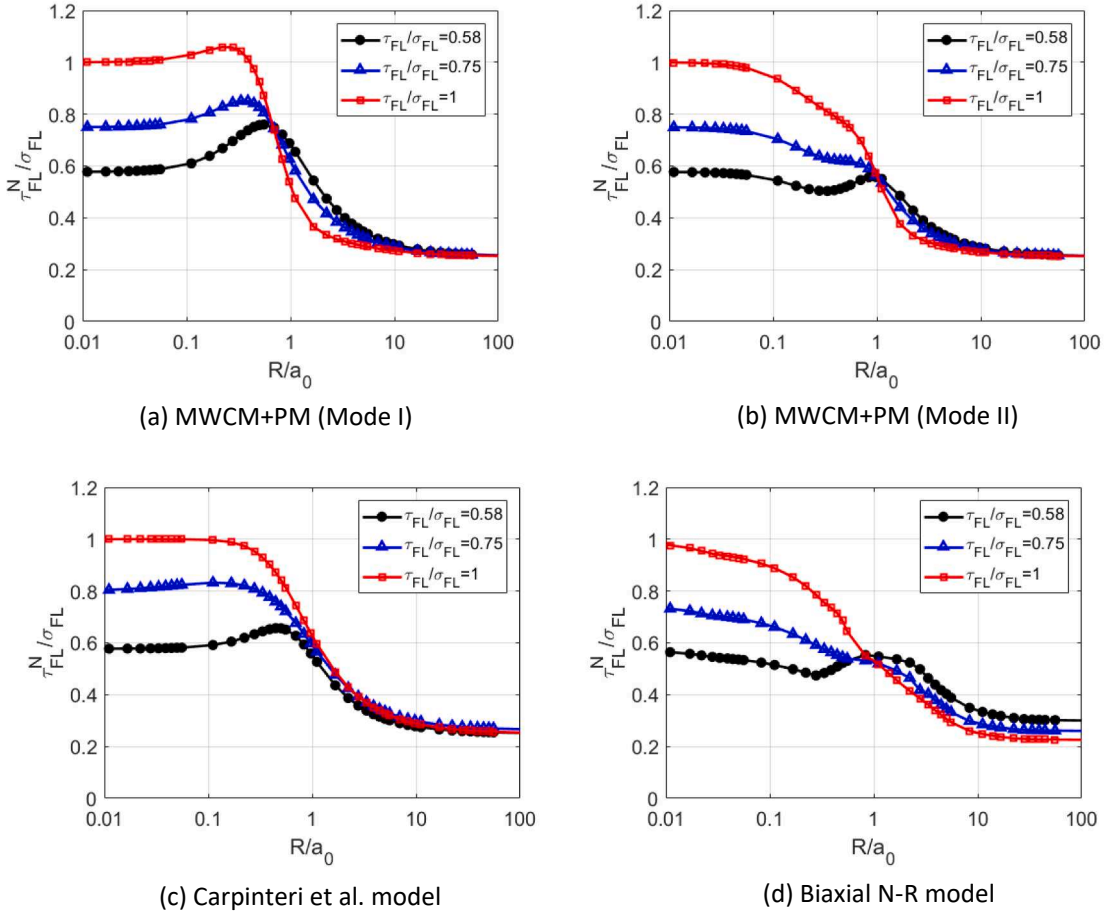

Fig. 5. Fatigue limit predictions for an infinite plate with a circular hole subjected to shear cyclic loading with several models: (a) MWCM + PM (Mode I) model, (b) MWCM + PM (Mode II) model, (c) Carpinteri et al. model and (d) Biaxial N-R model.

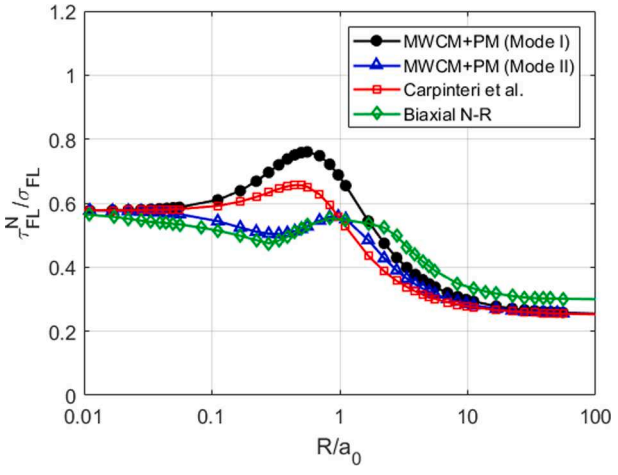

Fig. 6. Fatigue limit predictions of several models for a material with $\tau_{FL}/\sigma_{FL} = 0.58$ for an infinite plate with a circular hole subjected to shear cyclic loading.

arises from the non-monotonic evolution of the stress σ_{rr}. Deriving the expression of τ_a in Eq.Eqn 9 and setting it to zero, the minimum of τ_a is obtained, which is located at $r/R = 1.73$ and has a value of $\tau_a = 0.67$.

From the value of τ_a at the critical distance $a_0/2$ from the hot spot for a unitary applied load, which we call $\tau_a(a_0/2)$, the notch fatigue limit in torsion τ^N_{FL} will be the value that multiplied by $\tau_a(a_0/2)$ gives a value equal to the plain fatigue limit in torsion τ_{FL}:

$$\tau_a\left(\frac{a_0}{2}\right)\cdot\tau^N_{FL} = \tau_{FL} \rightarrow \tau^N_{FL} = \frac{\tau_{FL}}{\tau_a\left(\frac{a_0}{2}\right)} \rightarrow \frac{\tau^N_{FL}}{\sigma_{FL}} = \frac{0.5}{\tau_a\left(\frac{a_0}{2}\right)} \tag{10}$$

According to this equation, the evolution of the dimensionless notch fatigue limit τ^N_{FL}/σ_{FL} is inverse to the evolution of $\tau_a(a_0/2)$. The evolution of τ^N_{FL}/σ_{FL} with respect to the dimensionless hole radius R/a_0 is shown in Fig. 10 for the case of shear and $\tau_{FL}/\sigma_{FL} = 0.5$. The curve begins from a value of 0.5 as R/a_0 tends to zero. For a typical value of a_0 of a few hundred microns, R/a_0 tending to zero implies that R also tends to zero, and $a_0/2R$ tends to infinity. Therefore, the prediction of τ^N_{FL}/σ_{FL} as R/a_0 tends to zero is made with the value of τ_a corresponding to r/R tending to infinity, which, according to Fig. 9, is $\tau_a = 1$. Applying Eq. Eqn 10, τ^N_{FL}/σ_{FL} is equal to 0.5/1 = 0.5, which is precisely the value of τ^N_{FL}/σ_{FL} indicated above. Continuing with the analysis of the evolution of τ^N_{FL}/σ_{FL}, the curve rises from 0.5 to a maximum value of 0.75 for $R/a_0 = 0.68$; that is, for $a_0/2 = 0.73R$. This maximum value is obtained using the value of τ_a corresponding to r/R = 1.73, i.e. 0.67, which is precisely the minimum of the evolution of τ_a, as seen in Fig. 9. Again, if Eq. Eqn 10 is used, τ^N_{FL}/σ_{FL} is equal to 0.5/0.67 = 0.75, as shown in Fig. 10. Therefore, the ascending evolution of τ^N_{FL}/σ_{FL} from 0.5 to 0.75, for R/a_0 from 0 to 0.68 corresponds to the descending evolution of τ_a, for r/R from infinity to 1.73. The increase in the variable R/a_0 used in the graph of Fig. 10 implies a decrease in the variable r/R used in the graph of Fig. 9. Finally, the curve of τ^N_{FL}/σ_{FL} decreases from the maximum value of 0.75, tending to 0.25 as R/a_0 tends to infinity. This descending part of the τ^N_{FL}/σ_{FL} curve up to a value of 0.25 corresponds to the part of the τ_a curve from $r/R = 1.73$ to $r/R = 1$, where it reaches a value of $\tau_a = 2$. Again, if Eq. Eqn 10 is

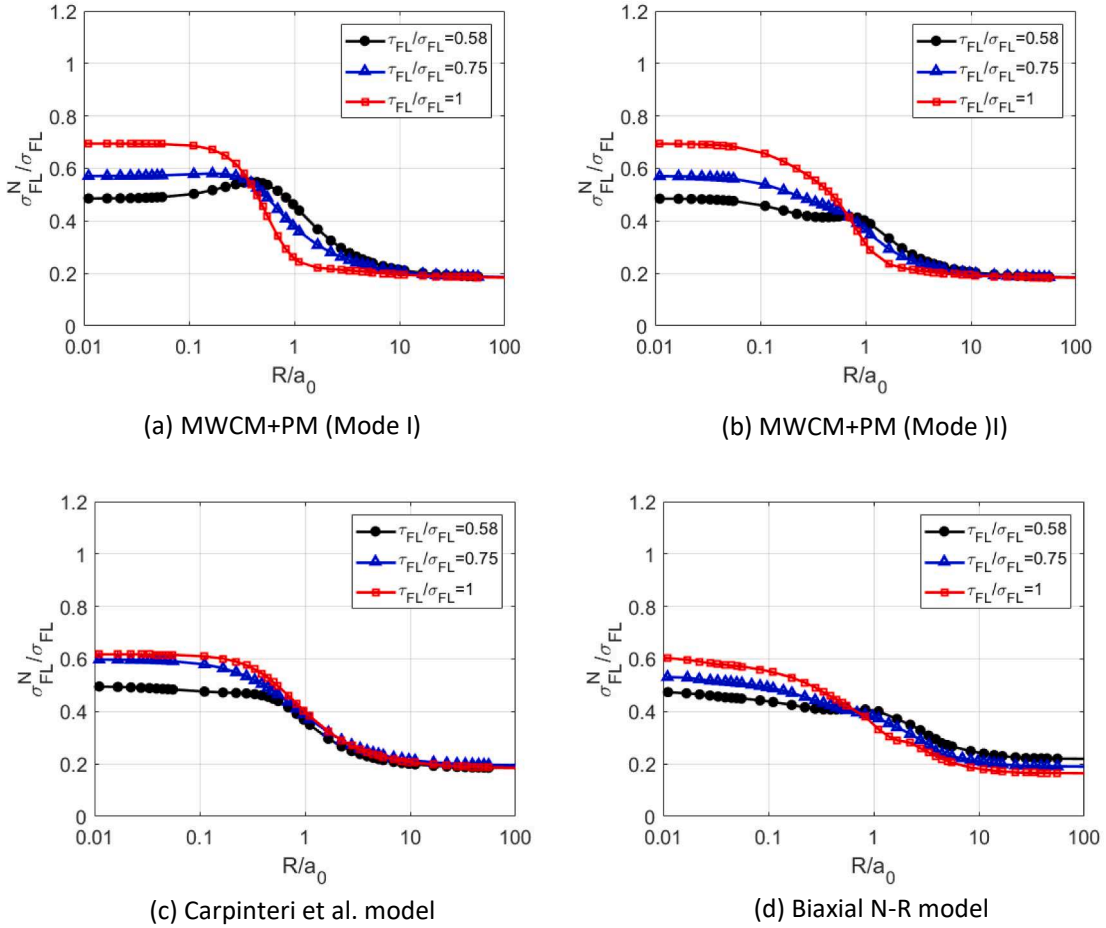

Fig. 7. Fatigue limit predictions for an infinite plate with a circular hole subjected to in-phase biaxial cyclic loading ($\sigma_y^\infty = \tau^\infty$). with several models: (a) MWCM + PM (Mode I) model, (b) MWCM + PM (Mode II) model, (c) Carpinteri et al. model and (d) Biaxial N-R model.

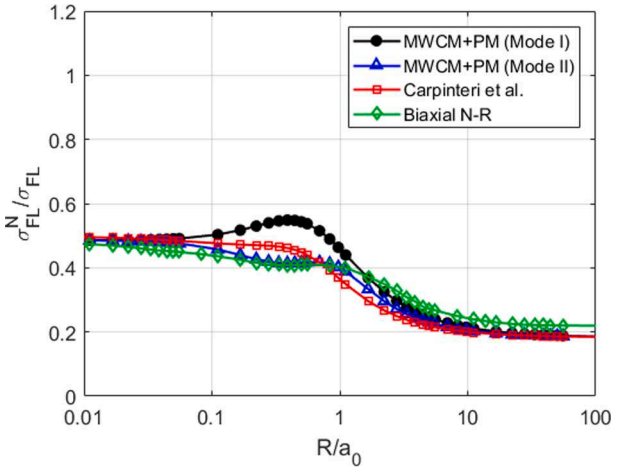

Fig. 8. Fatigue limit predictions of several models for a material with $\tau_{FL}/\sigma_{FL} = 0.58$ for an infinite plate with a circular hole subjected to in-phase biaxial cyclic loading ($\sigma_y^\infty = \tau^\infty$).

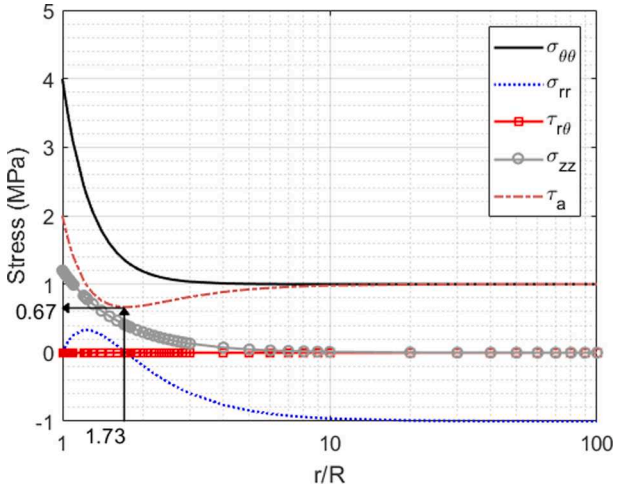

Fig. 9. Stresses evolution over the line $\theta = \theta_1 = 45^\circ$, for shear loading $\tau^\infty = -1$ MPa.

used, a value of $\tau^N_{FL}/\sigma_{FL} = 0.5/2 = 0.25$ is obtained, as expected. In summary, it is the rise and fall on the evolution of the stress σ_{rr} along the line $\theta = \theta_1 = 45^\circ$ that produces the fall and rise of the stress τ_a along the same line, which causes the rise and fall, i.e. the hump, in the evolution of the MWCM + PM (Mode I) predictions for the case of shear and a material with $\tau_{FL}/\sigma_{FL} = 0.5$, as shown in Fig. 10.

For the same model and the same loading (shear), but for materials with $\tau_{FL}/\sigma_{FL} \neq 0.5$, the situation changes since the second term, which we call *term2*, on the left side of the fatigue criterion (Eq. (1)), i.e. $(\tau_{FL} - \sigma_{FL}/2) \bullet (\sigma_{n,max}/\tau_a)$, is no longer zero. Again, if we know the values of τ_a and $\sigma_{n,max}$ at the critical distance $a_0/2$ from the hot-spot for a

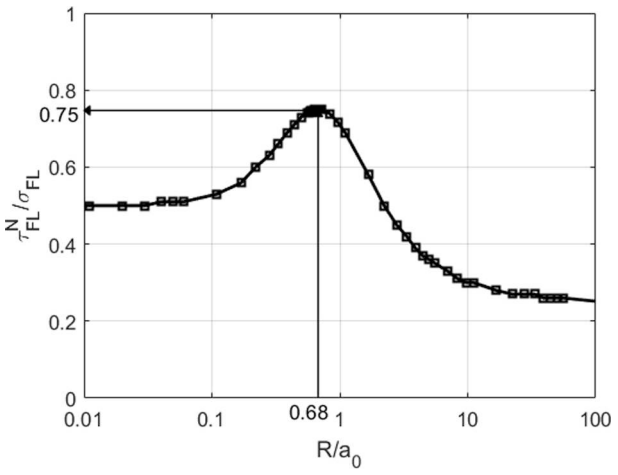

Fig 10. Notch fatigue limit evolution for a plate with a circular hole subjected to cyclic shear loading and a material with $\tau_{FL}/\sigma_{FL} = 0.5$ with the MWCM + PM (Mode I) model.

unitary applied load, which we call $\tau_a(a_0/2)$ and $\sigma_{n,max}(a_0/2)$, and the term2 formed with these two stresses, which we call term2$(a_0/2)$, then the notch fatigue limit will be the value that multiplied by $\tau_a(a_0/2)$ and $\sigma_{n,max}(a_0/2)$ fulfills the criterion of Eq. Eqn 1, that is:

$$\tau_a\left(\frac{a_0}{2}\right)\cdot\tau_{FL}^N + \left(\tau_{FL} - \frac{\sigma_{FL}}{2}\right)\frac{\sigma_{n,max}\left(\frac{a_0}{2}\right)\cdot\tau_{FL}^N}{\tau_a\left(\frac{a_0}{2}\right)\cdot\tau_{FL}^N} = \tau_{FL} \Rightarrow$$

$$\Rightarrow \tau_{FL}^N = \frac{\tau_{FL} - \left(\tau_{FL} - \frac{\sigma_{FL}}{2}\right)\frac{\sigma_{n,max}\left(\frac{a_0}{2}\right)}{\tau_a\left(\frac{a_0}{2}\right)}}{\tau_a\left(\frac{a_0}{2}\right)} \Rightarrow \frac{\tau_{FL}^N}{\sigma_{FL}} = \frac{\tau_{FL} - term2\left(\frac{a_0}{2}\right)}{\tau_a\left(\frac{a_0}{2}\right)\cdot\sigma_{FL}} \quad (11)$$

The combined stress term $\frac{\tau_a\left(\frac{a_0}{2}\right)\bullet\sigma_{FL}}{\tau_{FL}-term2\left(\frac{a_0}{2}\right)}$ of Eq. Eqn 11 is called τ_{comb} $(a_0/2)$. According to Eq. Eqn 11, the evolution of the dimensionless notch fatigue limit τ_{FL}^N/σ_{FL} for materials with $\tau_{FL}/\sigma_{FL} \neq 0.5$ is inverse to the evolution of τ_{comb}, which is similar to the relationship between the notch fatigue limit τ_{FL}^N/σ_{FL} and τ_a for the materials with $\tau_{FL}/\sigma_{FL} = 0.5$ shown in Eq. Eqn 10. Fig. 11 shows the evolution of τ_{comb} (for $\tau_{FL}/\sigma_{FL} = 0.5, 0.58, 0.75, 1$), τ_a and $\sigma_{n,max}$ for an applied stress $\tau^\infty = -1$ MPa on the line $\theta = \theta_1 = 45^\circ$ as a function of r/R. The 4 curves of τ_{comb} begin with a value of 4 for $r/R = 1$; they then decrease to a minimum, and finally tend towards constant values of 1/0.5, 1/0.58, 1/0.75 and 1/1, respectively, i.e. $1/(\tau_{FL}/\sigma_{FL})$, as r/R tends to infinity. According to Eq. Eqn 11, and repeating the previous reasoning used for Eq. Eqn 10, the value of $\tau_{comb} = 4$ as $r/R = 1$, implies that $\tau_{FL}^N/\sigma_{FL} = 1/4 = 0.25$ as R/a_0 tends to infinity, as shown in Fig. 5(a). The value of $\tau_{comb} = 1/\tau_{FL}$ as r/R tends to infinity, implies that $\tau_{FL}^N/\sigma_{FL} = \tau_{FL}$ as R/a_0 tends to 0, as shown in Fig. 5 (a). As explained above for τ_a, the falling and rising of these τ_{comb} curves correspond to the rising and falling in the curves of the model predictions, as shown in Fig. 5(a). The deepest trough of τ_{comb} occurs for a material with $\tau_{FL}/\sigma_{FL} = 0.5$, and becomes smoother as the τ_{FL}/σ_{FL} value increases. The explanation must be sought in the evolution of τ_a and $\sigma_{n,max}$ shown in Fig. 11, the first having a well-defined minimum while the second is monotonically decreasing. As the value of τ_{FL}/σ_{FL} increases, the weight of $\sigma_{n,max}$ increases with respect to τ_a in the combined stress τ_{comb}, which causes the valley of τ_{comb} to become shallower and almost disappear for materials with $\tau_{FL}/\sigma_{FL} = 1$. For this type of material the hump in the model predictions is very small, as shown in Fig. 5(a). In summary, the non-monotonic evolution of τ_a causes the humps of the MWCM + PM model (Mode I) prediction curves for shear loading. For higher values of τ_{FL}/σ_{FL}, the weight of τ_a versus $\sigma_{n,max}$ decreases in the prediction, causing the size of the hump to decrease.

Fig. 12 shows the evolution of the stresses $\sigma_{\theta\theta}$, σ_{rr}, τ_a, $\sigma_{n,max}$ and τ_{comb} in the line $\theta = \theta_1 = 0^\circ$ as a function of r/R, for the case of axial loading ($\sigma_y^\infty = 1$ MPa). This line is the crack path used for predictions with the MWCM + PM model (mode I) for this loading. The evolution of $\sigma_{\theta\theta}$ is similar to the case of shear (Fig. 9), which is monotonically decreasing. The great difference with respect to shear is in σ_{rr}: it increases from 0 MPa to 0.37 MPa, similar to the case of shear, which increases from 0 MPa to 0.33 MPa. However, the descent from this maximum is much smoother in the axial case than in the shear case, tending to 0 MPa as r/R tends to infinity, instead of to −1 MPa as it occurs in the shear case. Due to the gentler evolution of σ_{rr}, τ_a is almost a monotonically decreasing function, with a very smooth valley. For this reason, the hump for $\tau_{FL}/\sigma_{FL} = 0.58$ is much smaller for axial loading (3(a)) than for shear loading (5(a)). For higher values of τ_{FL}/σ_{FL}, such as $\tau_{FL}/\sigma_{FL} = 0.75$, the hump disappears completely due to the influence of $\sigma_{n,max}$, which makes the τ_{comb} monotonically decrease. For very high τ_{FL}/σ_{FL}, such as $\tau_{FL}/\sigma_{FL} = 1$, a greater influence of $\sigma_{n,max}$ even produces a hump in the evolution of τ_{comb}. The τ_{comb} hump produces the valley observed in the evolution of the model prediction for $\tau_{FL}/\sigma_{FL} = 1$, as shown in Fig. 3(a). In summary, the smoother evolution of the stress σ_{rr} along the line $\theta = \theta_1 = 0^\circ$, for axial loading, as compared to its evolution along the line $\theta = \theta_1 = 45^\circ$ for shear loading, essentially to fulfill the boundary conditions of the problem at infinity, produces a smoother evolution of the stress τ_a, which causes less pronounced humps in the evolution of the predictions

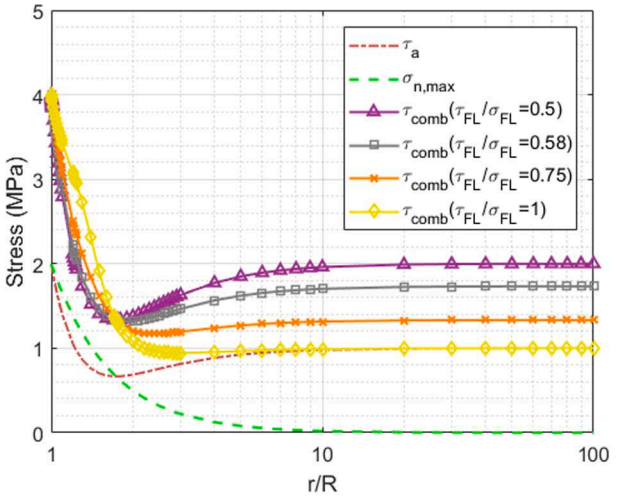

Fig. 11. Combined stresses evolution used in the MWCM + PM (Mode I) model for several materials over the line $\theta = \theta_1 = 45^\circ$, for shear loading ($\tau^\infty = -1$ MPa).

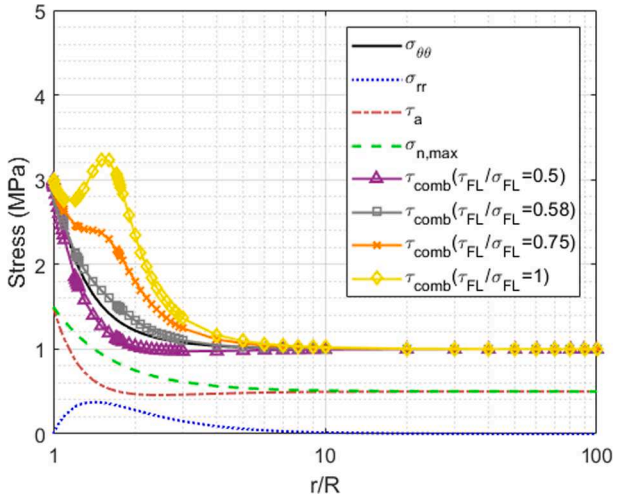

Fig. 12. Stresses evolution used in the MWCM + PM (Mode I) model criterion for several materials over the line $\theta = \theta_1 = 0^\circ$, for axial loading ($\sigma_y^\infty = 1$ MPa).

with the MWCM + PM (Mode I) model, as compared to the shear case.

For in-phase biaxial cyclic loading ($\sigma_y^\infty = \tau^\infty$), the evolution of the predictions of the MWCM + PM (Mode I) model (Fig. 7(a)) is intermediate between the evolution shown for axial loading (Fig. 3(a)) and shear loading (Fig. 5(a)), with small humps for $\tau_{FL}/\sigma_{FL} = 0.58,\ 0.75$ and no valley for $\tau_{FL}/\sigma_{FL} = 1$. Again the explanation of this evolution lies in the stresses along the path used for the predictions, in this case the line $\theta = \theta_1 = 32^\circ$, as shown in Fig. 13, for $\sigma_y^\infty = -\tau^\infty = 1$. σ_{rr} presents an intermediate evolution with respect to the axial and shear case. As an example, observe its trend as r/R tends to infinity, tending to −0.62 MPa, which is an intermediate value between 0 MPa (value for the axial case) and −1 MPa (value for the shear case). This generates an intermediate evolution of τ_a, between the axial and shear evolution, with a smooth valley that is less pronounced than in shear, and very smooth valleys in the evolution of τ_{comb}, without having any humps as in the axial case and $\tau_{FL}/\sigma_{FL} = 1$.

4.2. Elastic stress analysis for the MWCM + PM (Mode II) model

The evolution of the MWCM + PM (Mode II) model predictions, shown in Figs. 3(b), 5(b) and 7(b), presents fewer humps and is smaller than that of the previously analysed MWCM + PM (Mode I). The curves in Figs. 3(b), 5(b) and 7(b) monotonically decrease, except for the material $\tau_{FL}/\sigma_{FL} = 0.58$ and the cases of shear loading (Fig. 5(b)) and in-phase biaxial loading ($\sigma_y^\infty = \tau^\infty$) (Fig. 7(b)), with the rise and fall being almost imperceptible in this second case. The explanation for the evolution of the predictions is found, again, in the evolution of the elastic stresses used in the predictions. In the Mode II variant, the point at $L/2$ is on the line that forms 45° with the line normal to the surface at the hot-spot. Fig. 14 shows the prediction point using the Mode II variant for the case of shear, defined with polar coordinates (r, β). The stresses at this prediction point calculated with the Kirsch expressions include a nonzero shear stress term, except for a hole radius R tending to infinity, for which the prediction point has polar coordinates $r = R$ and $\beta = 45^\circ$. This is an important difference with respect to the Mode I variant, which, as we saw previously, has the prediction point at the line $\beta = 45^\circ$ for any hole radius R, and always has a zero value of the shear stress. Fig. 15(a) shows the evolution of the elastic stresses used for the predictions with Mode II variant versus the position of the prediction point. For hole radii R between 0 and infinity, a shear load $\tau^\infty = -1$ MPa and the same value of a_0 used previously ($a_0 = 0.18$ mm). For each value of R, the polar coordinates (r, β) of the prediction point were calculated and its stresses were obtained from the Kirsch expressions. To facilitate a comparison with Mode I variant, the position of the prediction point was expressed by the dimensionless variable r/R. Please note that the r value of the prediction point will be different for the Mode I variant and the Mode II variant, since the prediction point of each variant lies on different lines. For values of R/a_0 tending to zero the prediction point is at r/R tending to infinity and for values of R/a_0 tending to infinity the prediction point is at r/R tending to 1. As seen in the graph, $\sigma_{\theta\theta}$ has a decreasing evolution, from 4 MPa to 0 MPa, instead of to 1 MPa, as was the case for Mode I variant. σ_{rr} has a non-monotonic evolution, with a maximum of 0.31 MPa and tends to 0 at both ends, not to 0 and 1 at the ends, as was the case for Mode I variant. Finally, $\tau_{r\theta}$ is different from zero and progresses from 0 to 1 MPa. Despite the clear difference in the evolution of these stresses, the evolutions of the stresses used in the criterion, τ_a and $\sigma_{n,max}$, are quite similar in both variants, with τ_a going from 2 MPa to 1 MPa with a valley in between, and $\sigma_{n,max}$ monotonically decreasing from 2 to 0 MPa. As seen in Fig. 5(a) and (b), the predictions with the two variants tend to the same values at the extremes; however, they present differences in the central part, in the vicinity of $R/a_0 = 1$, with larger humps for Mode I variant. This difference in the central part is essentially due to the difference in the τ_a valley, which is smoother for Mode II variant. As seen previously, a smooth valley in τ_a causes little hump for materials with τ_{FL}/σ_{FL} close to 0.5 and no humps for materials with τ_{FL}/σ_{FL} close to 1.

Fig. 15(b) shows the evolution of the elastic stresses used for predictions with Mode II variant for axial load $\sigma_y^\infty = 1$ MPa. Again, there are differences in the evolution of the elastic stresses with respect to the evolution for Mode I variant: $\sigma_{\theta\theta}$ goes from 3 to 0.5 MPa instead of from 3 to 1 MPa, σ_{rr} goes from 0 to 0.5 MPa instead of from 0 to 0 MPa and $\tau_{r\theta}$ is different from 0. Despite this, the stresses used for the criterion, τ_a and $\sigma_{n,max}$, have the same values at the extremes for the two variants, 1.5 and 0.5 MPa, so the predictions of the two models converge to the same values at the extremes (Fig. 3(a) and (b)). Again, there is a certain difference in the predictions in the vicinity of $R/a_0 = 1$: for Mode II variant, all the curves are monotonically decreasing and relatively close to one another, while for Mode I variant, one of the curves has a hump and

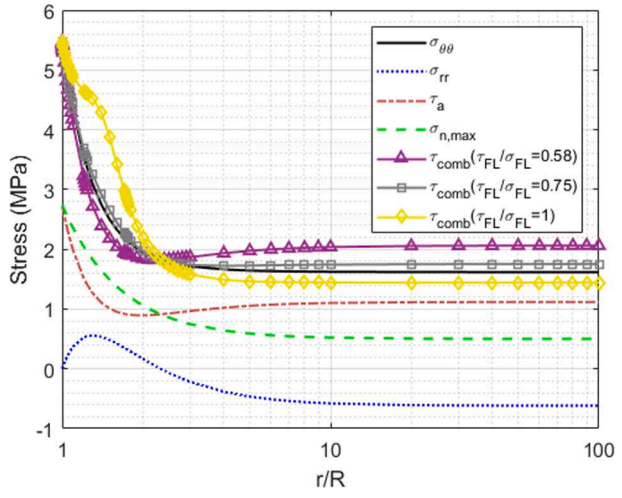

Fig. 13. Stresses evolution used in the MWCM + PM (Mode I) model criterion for several materials over the line $\theta = \theta_1 = 32^\circ$, for biaxial loading ($\sigma_y^\infty = -\tau^\infty = 1$ MPa).

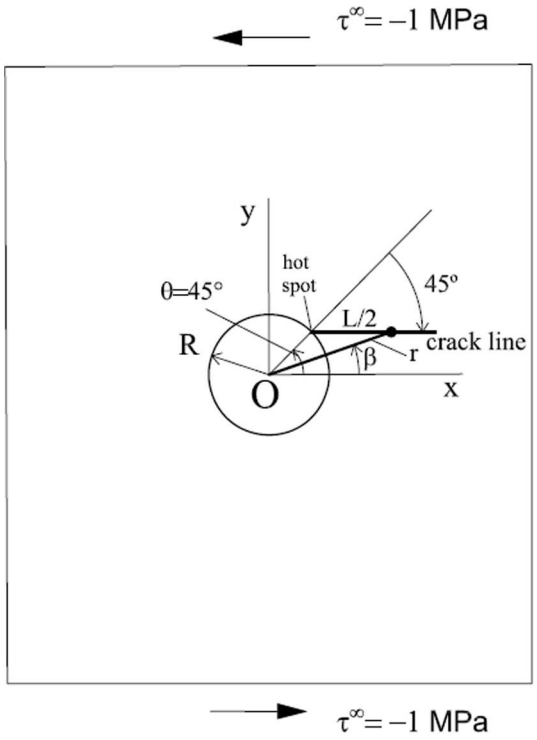

Fig. 14. Crack line for the the MWCM + PM (Mode II) model for shear cyclic loading ($\tau^\infty = -1$ MPa).

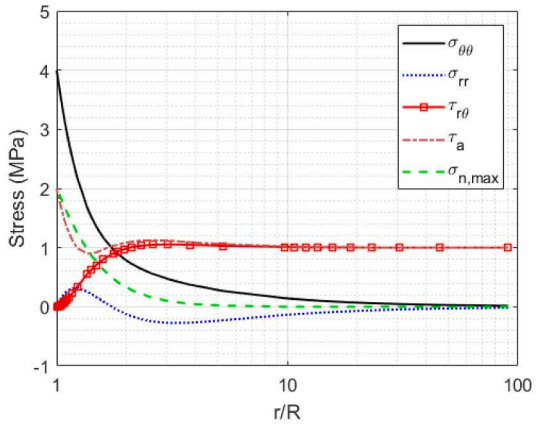

(a) Shear

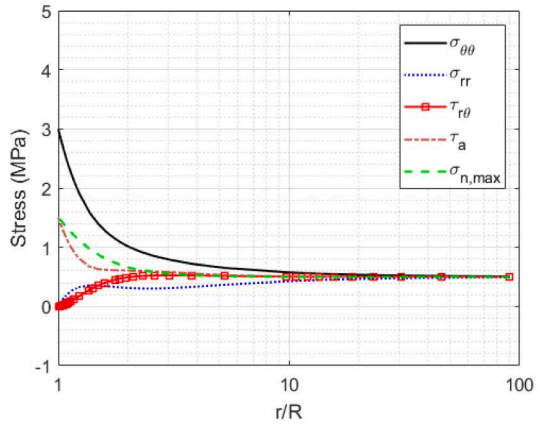

(b) Axial

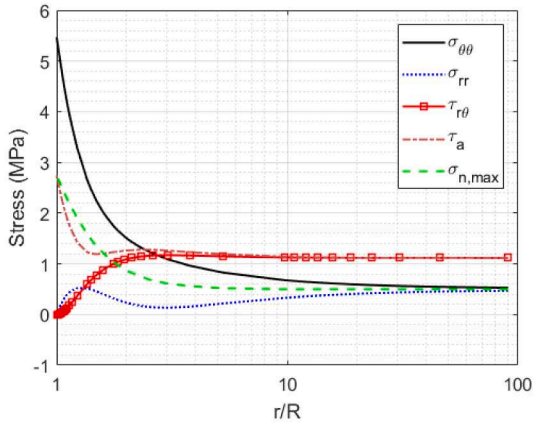

(c) Biaxial

Fig. 15. Stresses evolution at the prediction point used in the MWCM + PM (Mode II) model for: (a) shear loading ($\tau^{\infty} = -1$ MPa), (b) axial loading ($\sigma_y^{\infty} = 1$ MPa) and (c) biaxial loading ($\sigma_y^{\infty} = -\tau^{\infty} = 1$ MPa).

another has a valley, which are far apart. The monotonically decreasing evolution in Mode II variant's predictions is related, as we have seen before, with the monotonically decreasing evolution of τ_a without any valley in the entire domain. The greater closeness of the prediction curves for the Mode II variant versus Mode I variant in axial loading is related to the greater closeness of the τ_a and $\sigma_{n,max}$ curves. Focusing on the values of r/R close to 1.5, which correspond to values of R/a_0 close to 1, the greater the distance between $\sigma_{n,max}$ and τ_a for Mode I variant, causes a slight increase in the $\sigma_{n,max}/\tau_a$ ratio. This causes for values of τ_{FL}/σ_{FL} close to 1, *term2* to approach 1, and therefore, the denominator of τ_{comb}, that is, $\tau_{FL} - term2$, approaches 0, which makes the value of τ_{comb} increase considerably with respect to their values for τ_{FL}/σ_{FL} close to 0.5. For this reason, the prediction curves for Mode I variant are far from one another in the vicinity of $R/a_0 = 1$ as compared to those for Mode II variant.

Fig. 15(c) shows the evolution of the elastic stresses used for the predictions with Mode II variant for an in-phase biaxial load $\sigma_y^{\infty} = -\tau^{\infty} = 1$ MPa, which allows us to explain the evolution of the predictions in Fig. 7(b). Again, although the elastic stresses $\sigma_{\theta\theta}$, σ_{rr} and τ_a are different from those shown in Fig. 13 for Mode I variant, the stresses used in the criterion, τ_a and $\sigma_{n,max}$, are similar in both variants, tending to the same values at the extremes. Therefore, the prediction curves are similar for both variants, tending to the same values at the extremes. The very small hump observed in Fig. 7(b) for the material $\tau_{FL}/\sigma_{FL} = 0.58$, where R/a_0 is close to 1, is related to the very small valley in τ_a for r/R close to 1.5 in Fig. 15(c). The prediction curves in Fig. 7(b) have close values in the central zone, for values of R/a_0 close to 1, the reason for which is that the values of τ_a and $\sigma_{n,max}$ are very close for values of r/R close to 1.5, as seen in Fig. 15(c).

4.3. Elastic stress analysis for the Carpinteri et al. model

The evolution of the predictions with the Carpinteri et al. model monotonically decreases for axial and biaxial loading, while for shear loading it presents humps, a small one for a material with $\tau_{FL}/\sigma_{FL} = 0.58$ and an almost imperceptible one for a material with $\tau_{FL}/\sigma_{FL} = 0.75$. Let us analyse the evolution of the stresses used in this model's criterion, N_{max} and C_a, at the prediction point as a function of r/R, and the model criterion itself to explain the existence of these humps. The two stresses are calculated from the elastic stresses $\sigma_{\theta\theta}$, σ_{rr}, $\tau_{r\theta}$ at a point at $L/2$ from the hot-spot. As explained for the MWCM model, using a fixed value of a_0 ($a_0 = 0.18$ mm), for values of R/a_0 tending to zero the prediction point is at r/R tending to infinity and for values of R/a_0 tending to infinity the prediction point is at r/R tending to 1. As already explained in the description of the model, the point is located on a line that depends on the material: the line of the Mode I direction for materials with $\tau_{FL}/\sigma_{FL} = 1$, which is the line used in Mode I variant; the line of the Mode II direction for materials with $\tau_{FL}/\sigma_{FL} = 0.58$, which is the line used in Mode II variant; and an intermediate line to the previous two for materials with intermediate values of τ_{FL}/σ_{FL}. Fig. 16 shows the evolution of the stresses $\sigma_{\theta\theta}$, σ_{rr}, $\tau_{r\theta}$, N_{max} and C_a for shear loading at the prediction point as a function of r/R for each of the three studied materials ($\tau_{FL}/\sigma_{FL} = 1, 0.75, 0.58$). Please note that the r value of the prediction point will depend on τ_{FL}/σ_{FL}, since the prediction line used in this model depends on τ_{FL}/σ_{FL}. For $\tau_{FL}/\sigma_{FL} = 1$ (Fig. 16 (a)), the normal stress N_{max} coincides with the stress $\sigma_{\theta\theta}$, which monotonically decreases between 4 and 1 MPa. The shear stress C_a coincides with the stress $\tau_{r\theta}$, which in this case is 0 for the entire domain. Therefore, the equivalent stress used in the criterion (Eq. (3)) coincides with the stress $\sigma_{\theta\theta}$. The monotonic evolution of this stress implies a monotonic evolution of the model's prediction for this case, as shown in Fig. 5(c). For materials with $\tau_{FL}/\sigma_{FL} \neq 1$, the tension N_{max} continues to monotonically decrease, but the tension C_a ceases to be 0, starting from a value $C_a = (\sigma_{\theta\theta}/2)\sin(2\delta)$ as r/R tends to 1, and approaching $C_a = \tau_{r\theta}$ as r/R tends to infinity, to satisfy the boundary conditions at the edge of the

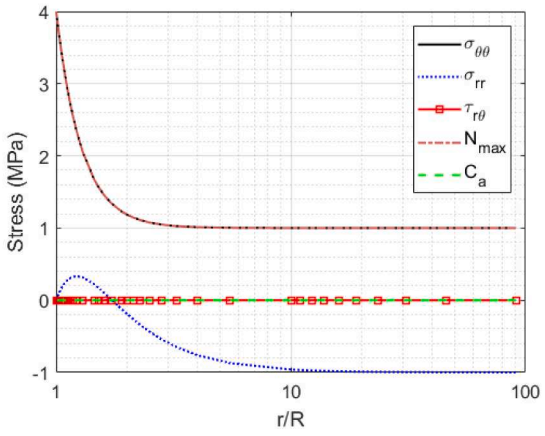

(a) $\tau_{FL}/\sigma_{FL} = 1$

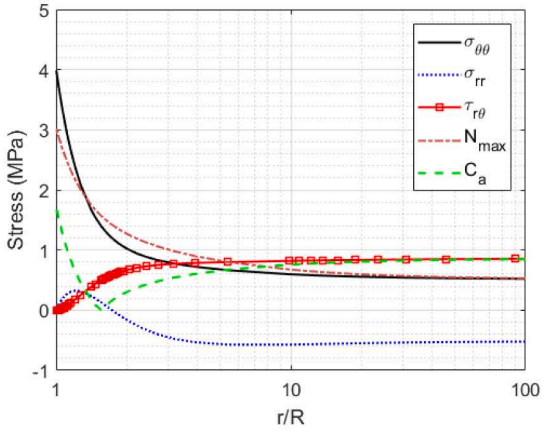

(b) $\tau_{FL}/\sigma_{FL} = 0.75$

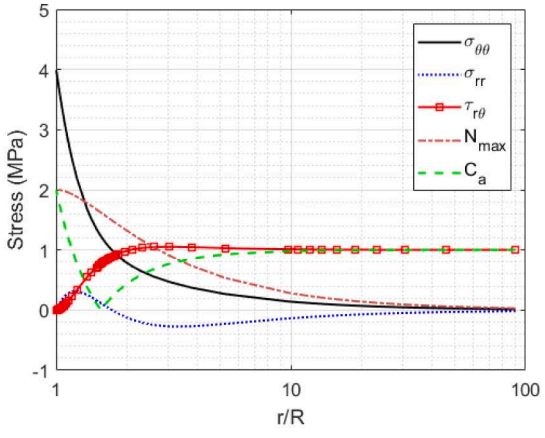

(c) $\tau_{FL}/\sigma_{FL} = 0.58$

Fig. 16. Stresses evolution at the prediction point used in the Carpinteri et al. model for shear loading ($\tau^{\infty} = -1$ MPa): (a) line $\theta = \theta_1 = 45°$ for a material with $\tau_{FL}/\sigma_{FL} = 1$, (b) line $\theta = 45°$, $\theta_1 = 15.47°$ for a material with $\tau_{FL}/\sigma_{FL} = 0.75$, (c) line $\theta = 45°$, $\theta_1 = 0°$ for a material with $\tau_{FL}/\sigma_{FL} = 0.58$.

hole and at infinity. The evolution of C_a does not monotonically decrease and has a valley with a minimum of 0 at approximately $r/R = 1.5$. The rise and fall are sharper for the material with $\tau_{FL}/\sigma_{FL} = 0.58$ compared to the material with $\tau_{FL}/\sigma_{FL} = 0.75$ since the values of the initial point and the horizontal asymptote are higher, i.e. 2 and 1 versus 1.71 and 0.86. Furthermore, in the fatigue criterion, the stress Ca is multiplied by a greater factor for the material with $\tau_{FL}/\sigma_{FL} = 0.58$ compared to the material with $\tau_{FL}/\sigma_{FL} = 0.75$, 1.73 versus 1.33. For these reasons, the fall and rise of C_a generates a rise and fall in the predictions, that is, a hump, for the material with $\tau_{FL}/\sigma_{FL} = 0.58$, this being almost negligible for the material with $\tau_{FL}/\sigma_{FL} = 0.75$.

For axial loading, the falls and rises of C_a are less acute than for shear loading in order to meet the boundary conditions at the ends so that no humps are generated. For an in-phase biaxial load $\sigma_y^{\infty} = -\tau^{\infty} = 1$ MPa, humps do not occur either, although the fall and rise of C_a are more acute than for shear loading. For this case, the N_{max} values are also higher and monotonically decreasing, compensating for the higher C_a values and preventing humps from occurring.

4.4. Elastic stress analysis for the biaxial N-R model

The evolution of the biaxial N-R model predictions monotonically decreases except for shear loading and the material with $\tau_{FL}/\sigma_{FL} = 0.58$(Fig. 5(d)), which has a hump near $R/a_0 = 1$, and for an in-phase biaxial load ($\sigma_y^{\infty} = \tau^{\infty}$) as well as the material with $\tau_{FL}/\sigma_{FL} = 0.58$, which has an almost imperceptible hump near $R/a_0 = 1$ (Fig. 7(d)). Again, the non-monotonic evolution of the stresses as a function of r/R used in this model provides an explanation for the existence of these humps. Although the stress analysis is more complicated than for the other models, the direction and length of the crack line used for the prediction can change for different radii, even if the material is not changed. Let us first study the shear loading and the extreme case of a material with$\tau_{FL}/\sigma_{FL} = 0.5$, for which the fatigue criterion is simplified, since the term $m^*_{\sigma 1} \bullet \tau_c$ tends to infinity (see Eq. (5)). The criterion adopts the following simplified expression:

$$\frac{\tau_3^i}{m^*_{\tau i} \cdot \tau_c} = 1 \tag{12}$$

Therefore, only the shear barrier stress τ_3^i, which is derived from the shear stress along the crack line, is used for the criterion. For shear loading and small holes, with R less than 0.15 mm and the usual properties of $d = 0.08$ mm and $a_0 = 0.18$ mm, direction of the crack line obtained with the model is $\theta = \theta_1 = 0°$. Fig. 17(a) shows the evolution of the radial stresses with r/R for this direction and an applied shear load $\tau^{\infty} = -1$ MPa. The stresses $\sigma_{\theta\theta}$, σ_{rr} are zero, while the stress $\tau_{r\theta}$ is not. For this case, the stress $\tau_{r\theta}$ is the shear stress in the crack line, which is used in the model to calculate the shear barrier stress τ_3^i. The analytical expression of $\tau_{r\theta}$ in this direction is the following:

$$\tau_{r\theta} = \tau^{\infty}\left(1 - 3\frac{R^4}{r^4} + 2\frac{R^2}{r^2}\right) \tag{13}$$

Starting from zero, it reaches a maximum value of 1.33 for $r/R = 1.73$ and finally tends to 1 as r/R tends to infinity. Its evolution is not monotonic and it is responsible for the non-monotonic evolution of the predictions. To verify this, the cases of two radii, $R = 0.05$ mm and $R = 0.1$ mm, are analysed. For both cases, the model predictions are made with the barrier stress in the first grain; that is, the first barrier requires a higher applied stress for the crack to overcome it, and thus it is the decisive barrier. According to previous works, for the first barrier a crack length of half a grain is used, that is, 0.04 mm, assuming that the average distance from the notch root to the first grain boundary is $d/2$. Fig. 17(b) shows the evolution of $\tau_{r\theta}$ in this first half of the grain for the two radii. The stress $\tau_{r\theta}$ for the radius $R = 0.05$ mm is above that of the radius $R = 0.1$ mm for the entire domain under study. For the radius $R = 0.05$ mm the stress reaches a maximum value of 1.33 MPa, while for

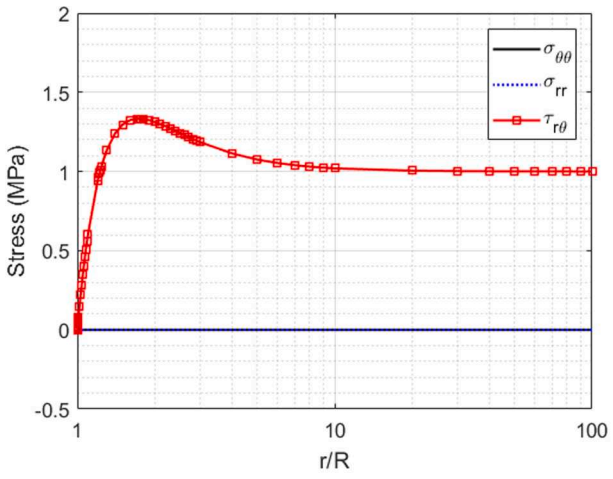

(a)

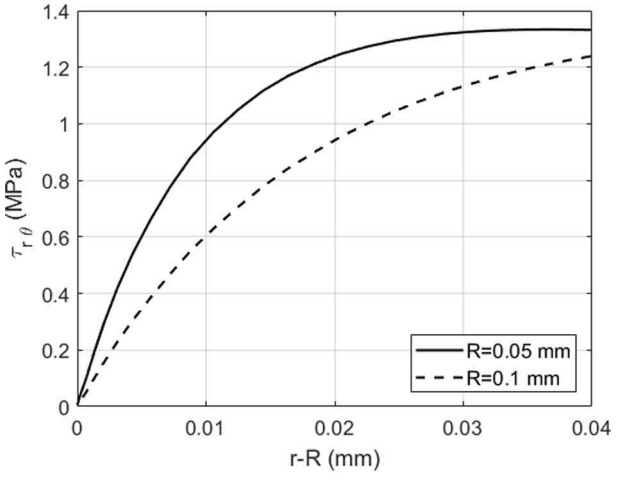

(b)

Fig 17. (a) Stresses evolution on the line $\theta = \theta_1 = 0°$ for shear loading ($\tau^{\infty} = -1$ MPa), used in the biaxial N-R model for very small holes and a material with $\tau_{FL}/\sigma_{FL} = 0.5$. (b) $\tau_{r\theta}$ evolution along the crack line in the first grain for two different hole radii.

$R = 0.1$ mm this value is not reached. In fact, to reach this maximum, R must be greater than 0.055 mm. The shear stress in the barrier, which is proportional to the stress in the crack line, is also higher for $R = 0.05$ mm than for $R = 0.1$ mm, with $\tau_3^1 = 5.30$ MPa versus$\tau_3^1 = 4.55$ MPa. Therefore, the fatigue limit calculated with Eq. (12) is lower for $R = 0.05$ mm ($R/a_0 = 0.28$) than for $R = 0.1$ mm ($R/a_0 = 0.56$), with $\tau_{FL}^N/\sigma_{FL} = 0.42$ MPa versus $\tau_{FL}^N/\sigma_{FL} = 0.49$ MPa. Therefore, an increase in the size of the hole implies an increase in the notch fatigue limit, leading to a hump in the prediction curve.

For a material with$\tau_{FL}/\sigma_{FL} = 1$ the fatigue criterion is also simplified, since the term $m_{\tau 1}^{*} \bullet \tau_c$ tends to infinity (see Eq. (6)). The simplified criterion is:

$$\frac{\sigma_3^i}{m_{\sigma i}^{*} \cdot \tau_c} = 1 \tag{14}$$

In this case, only the normal barrier stress σ_3^i, calculated from the normal stress to the crack line, is used for the criterion. For shear loading and small holes, with R less than 0.035 mm and the usual properties $d = 0.08$ mm and $a_0 = 0.18$ mm, the direction of the crack line according to the model is $\theta = \theta_1 = 45°$. The evolution of the radial stresses with r/R for this direction with an applied shear load $\tau^{\infty} = -1$ MPa was already shown in Fig. 9. The normal stresses to the crack line, used for the criterion, coincide with $\sigma_{\theta\theta}$, which has a monotonically decreasing evolution from 4 MPa to 1 MPa. Its analytical expression in this direction is:

$$\sigma_{\theta\theta} = -\tau^{\infty}\left(1 + 3\frac{R^4}{r^4}\right) \tag{15}$$

Its evolution is monotonic as is the evolution of the predictions. Again, the cases of two radii, $R = 0.015$ mm and $R = 0.030$ mm this time, are analysed to verify this model behaviour. For both radii, the model calculations indicate that the notch fatigue limits are calculated from the second barrier stress; that is, a crack length of $0.04 + 0.08 = 0.012$ mm is used to calculate the barrier stress and the notch fatigue limit. Fig. 18 shows the evolution of $\sigma_{\theta\theta}$ in the first one and a half grains for the two radii. In this case, the stress $\sigma_{\theta\theta}$ for the radius $R = 0.015$ mm is below that of the radius $R = 0.030$ mm for the entire domain, so it is the barrier stress, $\sigma_3^2 = 7.95$ MPa versus $\sigma_3^2 = 8.44$ MPa. The fatigue limit calculated with Eq. (14) is higher for $R = 0.015$ mm ($R/a_0 = 0.083$) than for $R = 0.030$ mm ($R/a_0 = 0.17$), $\tau_{FL}^N/\sigma_{FL} = 0.91$ MPa versus $\tau_{FL}^N/\sigma_{FL} = 0.86$ MPa. In this case, an increase in the hole radius implies a decrease in the notch fatigue limit; that is, a decreasing evolution, with no humps, as shown in Fig. 5(d) for this type of material.

Fig. 19 shows the N-R criterion left terms $\frac{\sigma_3^i}{m_{\sigma i}^{*} \cdot \tau_c} + \frac{\tau_3^i}{m_{\tau i}^{*} \cdot \tau_c}$ corresponding to the decisive barrier, that is, those used for the fatigue limit predictions, versus the dimensionless hole size, for an applied shear load $\tau^{\infty} = -1$ MPa and four materials; i.e. the two materials previously analysed and two intermediate materials. The inverse of these displayed values is directly the predicted dimensionless notch fatigue limit τ_{FL}^N/σ_{FL}. In this regards, "(d)" has been added to the barrier stresses σ_3^i and τ_3^i, to indicate that they correspond to the decisive barrier, i.e. $\frac{\sigma_3^i(d)}{m_{\sigma i}^{*} \cdot \tau_c} + \frac{\tau_3^i(d)}{m_{\tau i}^{*} \cdot \tau_c}$. For the material with $\tau_{FL}/\sigma_{FL} = 0.5$ the term $\frac{\sigma_3^i(d)}{m_{\sigma i}^{*} \cdot \tau_c}$ is zero and for the material with$\tau_{FL}/\sigma_{FL} = 1$ the term $\frac{\tau_3^i(d)}{m_{\tau i}^{*} \cdot \tau_c}$ is also zero, as explained before.

The direction of the crack line and the position of the barrier corresponding to the decisive barrier, defined by θ, θ_1 and i, change with the size of the hole and the material. Their values show certain trends, especially for very large or very small hole sizes and for materials with a single term in the criterion ($\tau_{FL}/\sigma_{FL} = 0.5, 1$), as shown in the previous explanations. However, in general it is very difficult to analyse their

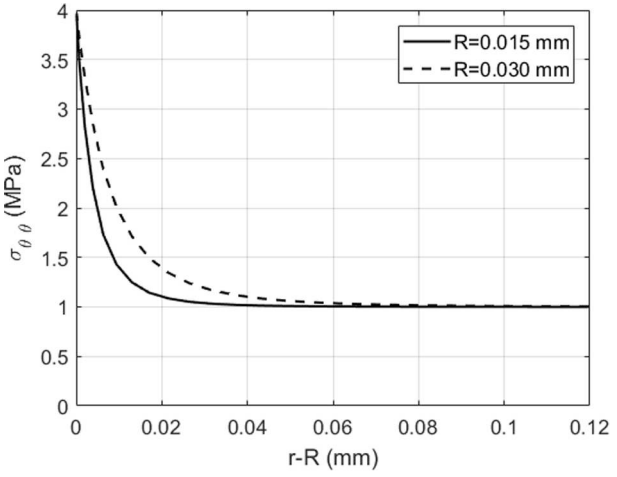

Fig 18. $\sigma_{\theta\theta}$ evolution along the crack line $\theta = \theta_1 = 45°$ in the first two grains for two different hole radii, used in the biaxial N-R model for shear loading ($\tau^{\infty} = -1$ MPa), very small holes and a material with $\tau_{FL}/\sigma_{FL} = 1$.

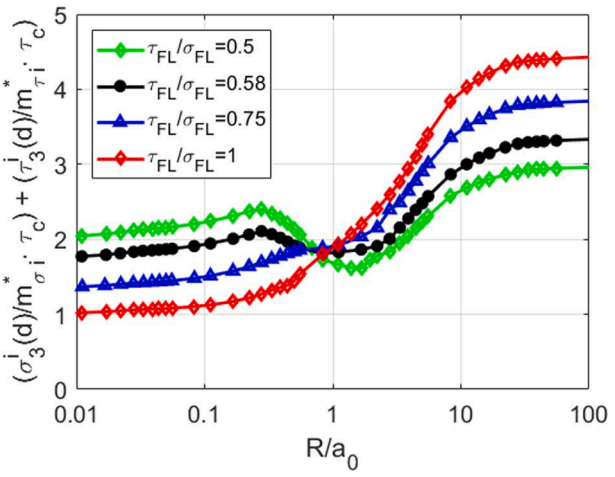

Fig 19. Decisive barrier stresses evolution used in the biaxial N-R model for shear loading ($\tau^\infty = -1$) MPa and four types of materials.

values for the decisive barrier, essentially because the number of combinations of these variables is very large, and the evolution of the shear and normal stresses in the crack line for non-radial directions from a circular hole is very complex. However, the evolution of the criterion terms shown in Fig. 19 does present a trend: all the curves have, in general, an increasing evolution, monotonically increasing for the material with $\tau_{FL}/\sigma_{FL} = 1$, with a large valley around $R/a = 1$ for the material with $\tau_{FL}/\sigma_{FL} = 0.5$, and with an intermediate behaviour between both for the materials with intermediate values of τ_{FL}/σ_{FL}. The increasing monotonic evolution for the material with $\tau_{FL}/\sigma_{FL} = 1$ is related to the use of only the σ_3^i stress in the criterion, which depends on the normal stresses in the crack line. The direction with the highest values of the stresses normal to the crack line, which will be the direction related to the decisive barrier, will be a direction with high values of the stress $\sigma_{\theta\theta}$, which has a monotonic evolution. On the other hand, for a material with $\tau_{FL}/\sigma_{FL} = 0.5$, only the stress τ_3^i is used in the criterion, which depends on the shear stresses in the crack line. In this case, the direction with the highest values of the shear stresses to the crack line will be a direction with high values of the stress $\tau_{r\theta}$, which has a non-monotonic evolution. Thus, the monotonic evolution of the stress $\sigma_{\theta\theta}$ and the non-monotonic evolution of the stress $\tau_{r\theta}$ provide a reasonable explanation for the monotonic and non-monotonic evolution of the curves for $\tau_{FL}/\sigma_{FL} = 1$ and $\tau_{FL}/\sigma_{FL} = 0.5$, respectively.

For materials with an intermediate value of τ_{FL}/σ_{FL}, the criterion includes the stresses σ_3^i and τ_3^i, with an increase in the weight of the stress τ_3^i with respect to the stress σ_3^i in the criterion as the τ_{FL}/σ_{FL} value of the material decreases. The quantitative analysis of the evolution of these curves is very complicated, although it is possible to qualitatively analyse this evolution. The material with $\tau_{FL}/\sigma_{FL} = 0.58$ has a higher weight for stress τ_3^i than the material with $\tau_{FL}/\sigma_{FL} = 0.75$, and therefore has a higher weight for the shear stress versus the normal stress in the crack line. As we have already seen, the shear stress is related to the stress $\tau_{r\theta}$, which has a non-monotonic evolution. That is why the material with $\tau_{FL}/\sigma_{FL} = 0.58$ has a hump while that with $\tau_{FL}/\sigma_{FL} = 0.75$ does not. However, the hump of the material with $\tau_{FL}/\sigma_{FL} = 0.58$ is not as pronounced as that of the material with $\tau_{FL}/\sigma_{FL} = 0.5$ due to the presence of the stress σ_3^i on the criterion. Similarly, the slope of the material with $\tau_{FL}/\sigma_{FL} = 0.75$ is not as steep as that of the material with $\tau_{FL}/\sigma_{FL} = 1$, due to the presence of the stress τ_3^i on the criterion. All the previous explanations could also be applied to justify the almost imperceptible jump in the case of biaxial load ($\sigma_y^\infty = \tau^\infty$) and the material with $\tau_{FL}/\sigma_{FL} = 0.58$, near $R/a_0 = 1$ (Fig. 7(d)). The evolution of the N-R criterion terms corresponding to the decisive barrier, i.e. $\frac{\sigma_3^i(d)}{m^*_{\sigma i}\cdot\tau_c} + \frac{\tau_3^i(d)}{m^*_{\tau i}\cdot\tau_c}$, is, again, generally monotonically increasing, although with a less steep slope than for the shear case. For the material with $\tau_{FL}/\sigma_{FL} = 0.58$, the evolution presents a very smooth valley near $R/a_0 = 1$, which corresponds to the small hump existing in the evolution of the fatigue limit prediction, as shown in Fig. 7(d).

5. Predictions of the experimental results from the literature

Several experimental results from the literature and the predictions of the presented models are compared in this section, to analyse the accuracy of the models and check if the humps predicted by the models are observed in reality. Experimental tests by Endo and Murakami, reported by Murakami in his book [11], by Endo [28,29] and by Chaves et al. [15,16] are analysed. The tests of Endo and Murakami dealt with 10 mm outer diameter round bars with drilled transverse surface holes made of 0.46% C annealed steel subject to fully reversed bending or torsion. The radii of the holes ranged from 0.02 to 0.25 mm [30]. Endo performed fully reversed axial, torsion and in-phase axial-torsion loading tests of 0.37% C steel round bars with drilled transverse surface holes with radii ranging from 0.05 to 0.25 mm. The specimen's outer diameter was 8.5 and 10 mm. The combined stress ratios of shear to normal applied stress $\tau^\infty/\sigma_y^\infty$ were chosen to be 0, 0.5, 1, 2, ∞. For both sets of tests the fatigue limit was defined for a lifetime of at least 10^7 cycles. Chaves et al. tested cylindrical specimens with an outside diameter of 16 mm and a thickness of 1.5 mm with a pass-through transverse hole made of AISI 304L stainless steel and 7075-T6 aluminium alloy. The radii of the holes were 0.5, 1 and 1.5 mm. The tests were fully reversed axial, torsional and in-phase axial–torsional. For stainless steel the fatigue limit was based on $3.5*10^6$ cycles to failure and for the aluminium alloy the endurance limit at 10^6 cycles was used. The fatigue properties of the studied materials are shown in Table 1, with the fatigue limits σ_{FL} and τ_{FL} expressed in terms of stress amplitude. The predictions of the models in this section were made using the properties shown in Table 1.

The elastic stress fields to make the predictions with the models were calculated with the analytical expression of Kirsch [25]. For the studied specimen's geometries, the effect of the curvature of the cylinder makes the stress field in the vicinity of the hole different from that of a hole in an infinite plate. Although if the cylinder is large enough and the transverse circular hole is small enough, then the difference in stresses in both cases becomes very small. For the cylindrical specimens tested by Chaves et al. [15,16], with an outside diameter of 16 mm, elastic studies for axial, torsional and biaxial loads ($\sigma_y^\infty = \tau^\infty$) indicated that for a circular hole with a radius not greater than 1.5 mm, the stress gradient ahead of the hole was very similar to the case of an infinite plate with a hole, being the difference in Kt less than 5% [32] The tested specimens had radii not greater than 1.5 mm, that is, fulfilling the conditions to

Table 1
Fatigue properties of literature materials.

Material	σ_{FL} (MPa)	τ_{FL} (MPa)	τ_{FL}/σ_{FL}	a_0 (mm)	Grain size, d (mm)	Reference
0.46% C steel	240	142	0.59	0.15 (a)	0.031 (b)	[11]
0.37% C steel	230	145	0.63	0.34 (a)	0.071 (b)	[28,29]
AISI 304L stainless steel	316	288	0.91	0.18	0.08	[15]
7075-T6 aluminium alloy	258	149	0.58	0.072 (c)	0.015	[16]

(a) [17].
(b) Estimated as $d = 2a_0/3.1^2$ (see [31]).
(c) Estimated as $a_0 = 3.1^2 d/2$ (see [31]).

have elastic fields close to the infinite case. In the case of the specimens tested by Murakami and Endo [11,28,29], the outer diameter of the specimen is smaller than 16 mm, between 8.5 and 10 mm, and therefore the curvature of the cylinder is greater. But the hole size is much smaller than 1.5 mm (with a maximum hole radius of 0.25 mm), more than compensating for the increase in curvature due to the specimen's diameter. So, for these geometries there is even greater similarity with the infinite plate case. In summary, in the analysis presented in this section, the simplification of using the analytical stress field of an infinite plate with a circular hole (Kirsch's equations) is reasonably justified.

For the models of Taylor and Susmel, and Carpinteri et al., plane strain was assumed. For the biaxial N-R model, the number of algebraic equations was set to 200 and the Kitawaga-Takahashi diagram was approximated with the equation proposed in [26], using f = 2.5. The experimental results, 33 in total, and the predictions with the models are shown in the Appendix. The fatigue limit prediction error was calculated as follows:

$$\text{Error} = 100*(\text{Prediction-Experimental})/\text{Experimental} \quad (16)$$

Fig. 20 shows the fatigue limit predictions with the four models versus the experimental notch fatigue limits. Error bands of ±20% have been included. Predictions within these bands are considered to have an acceptable error, according to Taylor [3] and Susmel [17]. For the four models, most predictions fall within the 20% error bands. Table 2 shows the statistics of the results calculated using the 33 results. The minimum average error is 9.1% for Carpinteri et al., followed by the MWCM + PM (Mode II) model and the biaxial N-R model, with 9.8% and 11.7%, respectively, and finally the MWCM + PM (Mode I) model with 15.5%. The absolute value of the errors was used to calculate the average error in order to prevent the positive and negative errors from compensating for one another. Regarding the percentage falling within the 20% error bands, which is the generally accepted margin of error for this type of prediction, Carpinteri's model is the best with 87.9%, followed by MWCM + PM (Mode II) model, with 84.8%, and finally MWCM + PM (Mode I) model and the biaxial N-R model, both with 75.8%. All the predictions with the MWCM + PM (Mode II) model have an error below the +20% band, which means that all these model predictions are acceptable or at least conservative. This percentage drops slightly for Carpinteri's model to 97.0% and drops further, to 87.8% and 84.8%, for the MWCM + PM (Mode I) model and N-R biaxial model, respectively.

Table 2
Statistics of the predictions with the four models.

Model	Average Error (%)	Percentage falling within ±20% error	Percentage with error < +20%
MWCM + PM (Mode I)	15.5	75.8	84.8
MWCM + PM (Mode II)	9.8	84.8	100
Carpinteri et al.	9.1	87.9	97.0
Biaxial N-R	11.7	75.8	87.9

The Murakami and Endo tests, for six hole radii between 0.02 and 0.25 mm and a material with a τ_{FL}/σ_{FL} value very close to that of von Mises, allow us to check whether the predicted evolution with the models, monotonically decreasing for an axial load and with a hump for

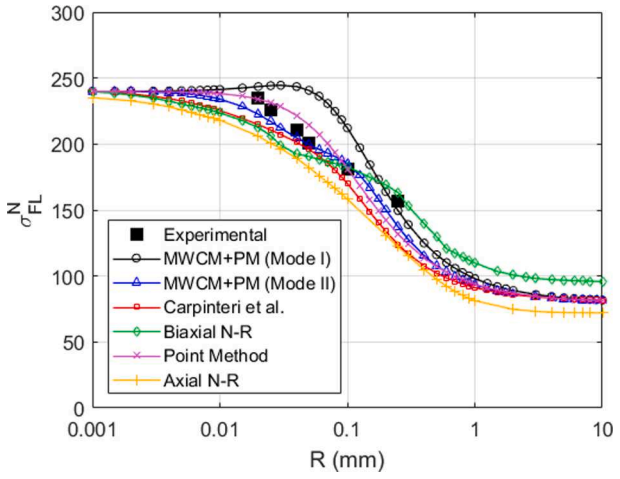

Fig 21. Experimental results obtained by Endo and Murakami [11] and model predictions for specimens with a circular hole subjected to cyclic axial loading. Material: 0.46% C annealed steel.

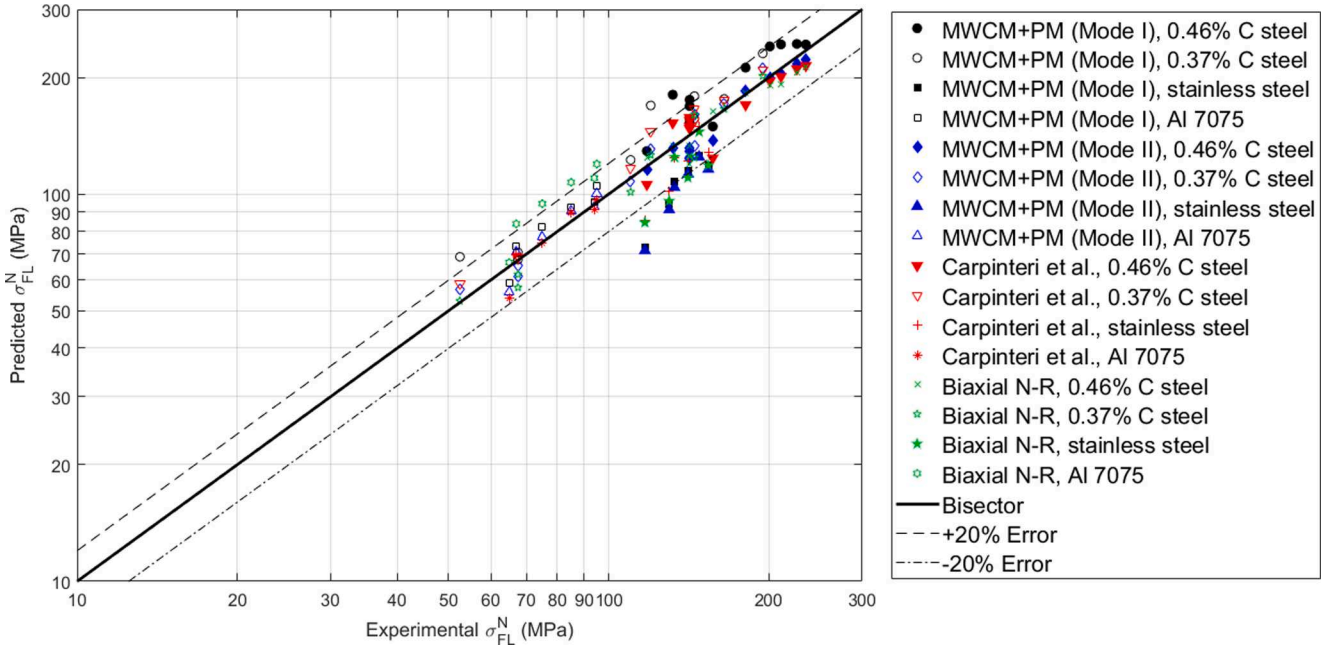

Fig. 20. Fatigue limit predictions with the models versus experimental fatigue limits for notched specimens.

a torsional load, is close to the experimental evolution. Figs. 21 and 22 show the evolution of the experimental and predicted fatigue limits versus the hole radius R for these tests for bending and torsional loading, respectively. In Fig. 21, predictions with the PM [3] and the axial N-R [6], which are axial models, are also included. In Fig. 21, the six experimental results have a decreasing monotonic evolution, as have the models. Certainly all the models capture the general tendency of the experimental results. For torsion (Fig. 22), the experimental results are the same for the four smallest radii, followed by a decreasing evolution, although not very marked, for the two largest radii. However, the hump predicted by the models, close to $R = 0.1$ mm, was not observed in the experimental results. The clearly different evolution of the results in torsion versus bending, with much less slope, may indicate that the non-monotonic evolution of the elastic stresses σ_{rr} and $\tau_{r\theta}$ when moving away from the hole contour (which are the cause of the hump in the models predictions for torsion) has a real effect on the experimental results, decreasing the slope of the curve, although it is not so important as to generate a hump in its evolution.

Fig. 23 shows the three experimental results of Endo [28,29] for the 0.37% C steel, a material with $\tau_{FL}/\sigma_{FL} = 0.63$, and biaxial loading $\tau^{\infty}/\sigma_y^{\infty} = 2$. The smooth decreasing monotonic evolution of the experimental results is close to that of the models, with the exception of the small hump predicted by the MWCM + PM (mode I) model at approximately $R = 0.1$ mm. However it is true that there are not enough experimental values close to $R = 0.1$ mm to fully confirm the nonexistence of the small hump.

For large hole radii, all the models give very similar predictions for any type of material, with an evolution very close to the horizontal. Chaves et al.'s experimental results for Al 7075 [16] allow an analysis of these predictions, although it would certainly be convenient to have had more experimental results, especially for biaxial loading, with just one result. Fig. 24 shows the results for this material and the load of the axial, torsional and biaxial $\tau^{\infty} = \sigma_y^{\infty}$ types. The predictions of the models are close to the experimental results, and the evolution of the experimental results for axial and torsional loads is close to the horizontal evolution, similar to the models.

No experimental results were found for very small holes, i.e. an R smaller than 0.01 mm. The expected result would be convergence to the plain fatigue limit as R tends to zero. As the model predictions approximately converge to the plain fatigue limit as R tends to zero (see Figs. 3–8), then it would be expected that their predictions for this range of radii would be approximately correct.

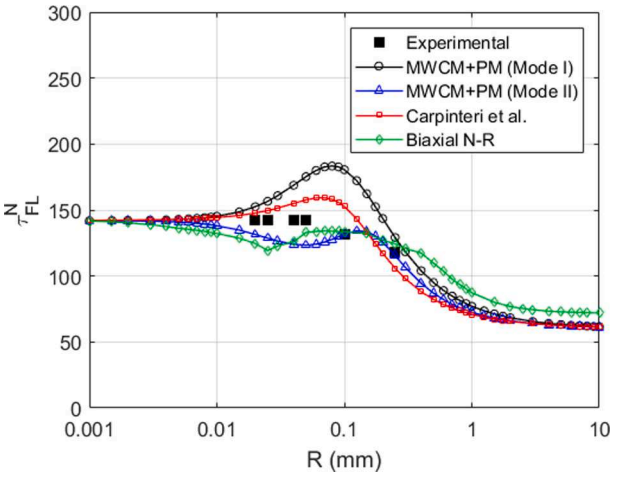

Fig 22. Experimental results by Endo and Murakami [11] and model predictions for specimens with a circular hole subjected to cyclic torsional loading. Material: 0.46% C annealed steel.

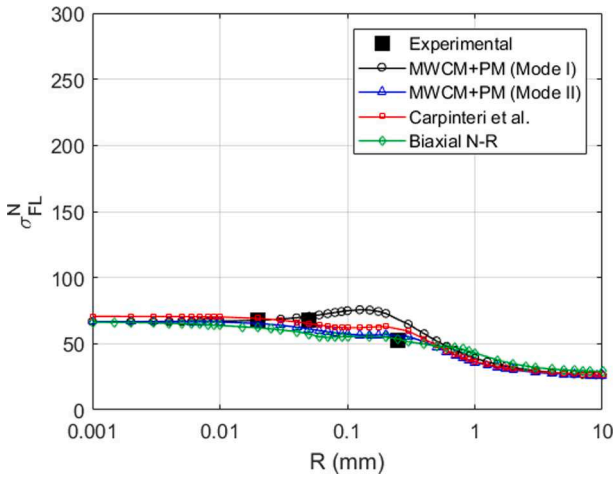

Fig. 23. Experimental results by Endo [28,29] and model predictions for the 0.37% C steel and the case of in-phase biaxial loading $\tau^{\infty}/\sigma_y^{\infty} = 2$.

6. Discussion

In this work, the fatigue limit prediction of various biaxial models for a circular hole were analysed, studying its evolution with an increase in the hole radius and making a comparison with experimental results from the literature. In general, model predictions were close to the results of the literature, with relatively low errors. Regarding the evolution of the predictions with the variation in the hole radius, all the models approximately converged to the plain fatigue limit for radii tending to zero and to the plain fatigue limit divided by K_t for radii tending to infinity, as expected. However, for intermediate radii the differences between the models were great, with so-called humps appearing, especially for torsional loading and ductile materials. The existence of these humps is due to the use in the fatigue criteria of stresses other than the stress $\sigma_{\theta\theta}$, such as σ_{rr} and $\tau_{r\theta}$, whose evolution with the increase in the variable r in the so-called crack line is non-monotonic. The larger or smaller size of the hump depends on the specific criteria of the model and the crack line used for the predictions, but in any case, it appears on all models. It seems that the only way to avoid the presence of these humps would be to substantially modify the criteria of the models. In the evolution of the experimental results for intermediate radii shown in the present work, which are the Endo and Murakami tests for axial and torsional loads, no humps were observed. However, a clearly different evolution was observed in these experimental results with respect to the hole radius for axial and torsional load, with much less of a slope for torsional load, which may indicate that the influence of the non-monotonic evolution of the elastic stresses σ_{rr} and $\tau_{r\theta}$ exists. However, the tests only involve six different radii and a single material, so no definitive conclusions can be drawn. There is currently no comprehensive set of experimental results in the literature for intermediate hole radii to ensure that humps do not occur. It seems clear that it would be necessary to perform a test campaign, sweeping a good number of intermediate radii for various materials to know if the humps actually occur or not.

The parametric study shown in Section 3 indicates that the hump effect occurs for a value of R/a_0 close to 1. Just to put this in context, according to a recent article [33], the average value of a_0 for 67 steels reported by Susmel in Appendix A of his book [17] is 0.141 mm, the maximum and minimum being 0.782 and 0.005 mm, respectively. So the humps occur, for the most common steels, for quite small hole sizes, clearly less than 1 mm. This implies that this hump effect does not affect normal components used in industry, where holes are typically several millimeters wide. However, in much smaller components, such as connectors employed in microelectronics chips or the stents used in coronary angioplasty, the humps described in the paper may play an

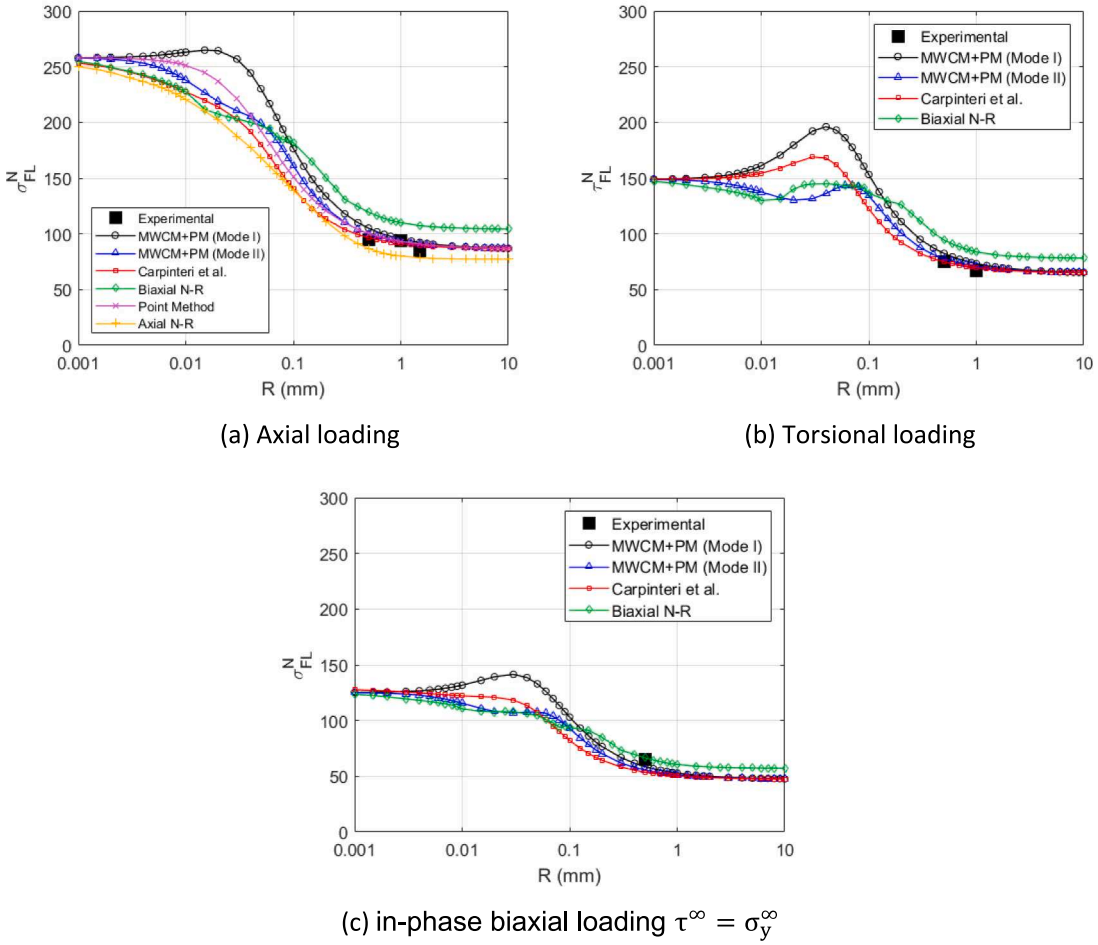

Fig. 24. Experimental results by Chaves et al. [16] and model predictions for the Al 7075: (a) axial loading), (b) torsional loading, and (c) in-phase biaxial loading $\tau^{\infty} = \sigma_y^{\infty}$.

important role, adding uncertainty to the predictions for these cases.

For the case of axial loading, predictions with specific models for this type of loading were included, such as the PM and the axial N-R model, providing different predictions with respect to those given by the biaxial models (see Fig. 4). A fundamental difference between these two types of models was that the predictions with the biaxial models depend on the torsional fatigue limit of the material, whereas this parameter does not affect the predictions with the axial models. A legitimate question is: which is more convenient to use for an axial load case, an axial model or a biaxial model? As seen in the prediction curves of the biaxial models in Fig. 4, the value of τ_{FL} clearly influences the predictions obtained with the MWCM + PM models, especially in the area of $R/a_0 = 1$. The influence of τ_{FL} is much less for Carpinteri et al. and the biaxial N-R models, and is obviously zero for the axial models. Conceptually, the question arises as to whether the torsional fatigue limit has an effect on the fatigue behaviour of a notched solid subject to fatigue axial loading. In addition, humps are not predicted with the axial models, since only the stress $\sigma_{\theta\theta}$ is used for the predictions, which has a monotonically decreasing evolution with respect to the hole radius. The average errors of the models' predictions for axial loading, with 13 cases studied, are shown in Table 3. The smallest average error occurs for an axial model, i.e. the PM (7.0%), but there is a biaxial model, that of Carpinteri et al., which also has a very low error (7.6%). The other studied axial model, the axial N-R, has the highest average error (13.1%). Thus, the analysed cases do not show a clear trend of the convenience of using an axial or biaxial model for axial loads. In any case, the number of hole radii and materials analysed are too few to be able to draw reliable conclusions.

Table 3
Statistics of the predictions with the models for the axial loading cases.

Model	Average Error (%)
MWCM + PM (Mode I)	12.7
MWCM + PM (Mode II)	8.5
Carpinteri et al.	7.6
Biaxial N-R	12.0
PM	7.0
Axial N-R	13.1

Again, it would be very convenient to conduct a campaign of fatigue axial tests in notched solids with several root radii made of materials with different τ_{FL} values. This would allow for the questions that have been raised to be answered, specifically, the effect (or lack thereof) of τ_{FL} and the existence (or lack thereof) of humps for the axial case.

Additionally, the diversity of directions used by the various models to make predictions is striking, from the Mode I direction to the Mode II direction, passing through intermediate values. This does not prevent the models from giving similar results for small and large radii, since they are essentially adjusted with the same parameters, the plain fatigue limits of the material. Again, it would be necessary to perform a comprehensive experimental analysis for various hole radii and various materials of the crack initiation point and the crack direction in its initial part in order to establish a single crack line to make predictions with all the models. In recent years, work has been performed in this field [15,16] but much work remains. Current knowledge indicates that the

experimental crack line is not straight, but instead zigzagged and changes direction when passing from Stage 1 to Stage 2. This implies that to improve the predictions, it would probably be necessary for current models to evolve towards the use of non-straight crack lines for prediction, which is closer to the experimental crack lines.

Though it is not possible to confirm the existence of these humps by reference to experimental data, it is interesting to speculate whether their existence is reasonable, considering the physical mechanisms involved. As is well known, fatigue proceeds in two stages, Stage 1 and Stage 2, which are loosely described as crack initiation and crack propagation. Previously, Susmel [21] showed that the length of the Stage-1 crack is similar to the critical distance in steel, which justifies the use of the TCD (combined with a critical plane theory) as a way of capturing the stresses acting during the initiation stage. We show in the present work that the stresses in this region, and especially the shear stress on the critical plane, vary in a complex way with distance from the hole, implying the existence of a hump in the fatigue limit predictions. From this we conclude that the existence of the hump could be consistent with the physical mechanisms of fatigue.

It is perhaps also worth noting that a similar effect has already been established in relation to the variation of strength with notch radius. Considering the variation of fracture strength (or measured fracture toughness) with root radius for notches of constant length, TCD predictions using the PM show a small decrease in strength with increasing radius for radii similar in magnitude to L. This counter-intuitive result has been shown to occur also in the experimental data for brittle fracture of some steels [3] and, recently, carbon fibre composite material [34]. It arises, in a similar way to that shown in the present work, due to a complex variation of stress with distance near the notch.

One striking thing the N-R model does not get right is the obvious difference it reports for pure axial loading between the biaxial formulation and the monoaxial formulation for the larger notches, as depicted in Fig. 4. It is clear the predictions with the biaxial formulation are wrong since they converge to a value $\sigma_{FL}^{N}/\sigma_{FL}$ of 0.4 rather than to the expected value around 1/3. The reason for this is the much simplified geometry the model uses for the slip band. In its present formulation, the crack growth direction is fixed from the initiation point onwards and does not change once it has been selected as the direction that maximizes the "pressure" upon the first microstructural barriers. The initiation direction is therefore set and taken to be the same for propagation until failure. This is to say that at present the model does not have the capability of reproducing the switch between stage I, mode II growth typically observed at initiation and stage II, mode I displayed later on. Current work is being done to incorporate the possibility of changes of direction in the propagation path, but the mathematical and numerical difficulties are great and no satisfactory strategy to come around these difficulties has yet been found.

Finally, the prediction curves of the N-R model are less smooth than those of the other models (see Figs. 3, 5 and 7). There are two reasons that can justify this behaviour of the N-R model. First, it is a model in which the equations are solved numerically; therefore there will always be a small numerical error when calculating the fatigue limit. Second, the N-R model is a discrete model, which bases its predictions on the analysis of a discrete set of crack directions and crack lengths. In this study an angular step of 1° was used for the crack directions. The discrete set of crack lengths corresponds to crack tips located at the successive grain boundaries.

7. Summary and conclusions

This work presented an analysis of the fatigue limit predictions for a plate with a circular hole subjected to cyclic axial, shear and in-phase biaxial loading through several biaxial models. There were clear differences between the models in terms of the crack initiation point and the crack line used for making the predictions. For small and large radii all the models gave similar predictions, tending to the plain fatigue limit and the plain fatigue limit divided by K_t as the hole radii tended to zero and infinity, respectively. For intermediate radii, there were considerable differences in the values of the predictions obtained with the models, despite the fact that this was a simple geometry. In some cases, and for all the models, increases in the notch fatigue limit were predicted with an increasing hole radius, especially in torsion, which is something that has not been observed experimentally, nor does it seem logical from a physical point of view. This non-monotonic evolution of the predictions with an increasing hole radius, called a hump, is also due to the non-monotonic evolution of the σ_{rr} and $\tau_{r\theta}$ stresses along the crack lines used in the models.

It would be very interesting to perform an exhaustive experimental work involving the fatigue testing of specimens with circular holes under several types of loading and including several materials. The tests should be focused on hole radii for which the models predict a non-monotonic evolution with the hole size, the so-called humps. For the tests, it would be very interesting to experimentally obtain the crack initiation point and the crack path in the initial part of the crack. Later, it would be convenient to adapt the crack lines used for the prediction in the current models to fit them as closely as possible to the experimentally observed crack paths. Additionally, the model criteria were adjusted to provide an evolution of the predictions with the hole radius close to that observed experimentally, either with or without humps. All this work would probably result in predictions of fatigue limits for notched specimens subjected to biaxial loading that are closer to the experimental values and, ultimately, provide the industry with better tools for predicting fatigue failure.

Declaration of Competing Interest

The authors declare that they have no known competing financial interests or personal relationships that could have appeared to influence the work reported in this paper.

Acknowledgements

The authors would like to thank the European Union, the Spanish Government and the Junta de Andalucía, Spain, for its financial support through grants DPI2017-84788-P and PID2020-117407 GB-I00 (FEDER/Ministerio de Ciencia e Innovación - Agencia Estatal de Investigación) and P18-FR-4306 ("Fondo Europeo de Desarrollo Regional (FEDER) y Consejería de Economía, Conocimiento, Empresas y Universidad de la Junta de Andalucía, dentro del Programa Operativo FEDER 2014–2020'').

Appendix

Experimental notch fatigue limits and predictions with the models.

Material	Ref.	Radius R (mm)	Type of loading	Notch fatigue limit									
				Experimental		MWCM+PM, Mode I		MWCM+PM, Mode II		Carpinteri et al.		Biaxial N-R	
			$\tau^\infty/\sigma_y^\infty$	σ_y^∞ (MPa)	τ^∞ (MPa)	σ_y^∞ (MPa)	τ^∞ (MPa)	σ_y^∞ (MPa)	τ^∞ (MPa)	σ_y^∞ (MPa)	τ^∞ (MPa)	σ_y^∞ (MPa)	τ^∞ (MPa)
0.46%C steel	[11]	0,02	0	235	0	243,5	0	222,6	0	214,7	0	212,5	0
		0,025	0	226	0	244,3	0	217,1	0	210,7	0	206,4	0
		0,040	0	211	0	243,6	0	204,7	0	201,3	0	192,5	0
		0,050	0	201	0	240,7	0	199,5	0	196,0	0	190,6	0
		0,100	0	181	0	212,2	0	184,9	0	170,1	0	182,9	0
		0,250	0	157	0	149,5	0	137,3	0	123,9	0	163,2	0
		0,020	∞	0	142	0	152,5	0	131,5	0	147,7	0	124,6
		0,025	∞	0	142	0	156,6	0	128,7	0	149,6	0	119,4
		0,040	∞	0	142	0	168,8	0	124,0	0	155,0	0	125,9
		0,050	∞	0	142	0	175,3	0	123,4	0	157,7	0	133,0
		0,100	∞	0	132	0	180,6	0	131,6	0	152,7	0	133,5
		0,250	∞	0	118	0	129,2	0	115,5	0	105,9	0	124,4
0.37%C steel	[28, 29]	0,050	0	195	0	230,9	0	212,0	0	209,8	0	202,0	0
		0,050	∞	0	145	0	156,5	0	132,8	0	154,3	0	124,3
		0,250	∞	0	120	0	169,4	0	130,3	0	144,7	0	126,2
		0,020	0,5	165	82,5	176,2	88,1	171,6	85,8	174,7	87,4	166,0	83,0
		0,050	0,5	145	72,5	179,1	89,5	160,7	80,3	166,2	83,1	160,2	80,1
		0,050	1	110	110	122,6	122,6	108,0	108,0	117,0	117,0	101,3	101,3
		0,020	2	67,5	135	67,7	135,4	65,4	130,7	68,9	137,8	62,0	124,0
		0,050	2	67,5	135	70,7	141,4	61,2	122,4	68,6	137,3	57,4	114,9
		0,250	2	52,5	105	68,9	137,9	56,6	113,1	58,9	117,7	53,0	105,9
Stainless steel	[15]	0,5	0	148	0	125,6	0	124,71	0	149,10	0	145,0	0
		1	0	154	0	118,4	0	116,01	0	128,59	0	118,7	0
		1,5	0	141	0	114,7	0	112,63	0	121,48	0	110,3	0
		0,5	∞	0	133	0	107,9	0	104,1	0	124,5	0	124,6
		1	∞	0	130	0	94,5	0	91,2	0	102,1	0	96,0
		0,5	1	117	117	73,1	73,1	71,5	71,5	85,7	85,7	84,5	84,5
Al 7075	[16]	0,5	0	95	0	105,1	0	100,1	0	96,6	0	119,6	0
		1	0	94	0	95,5	0	92,8	0	91,2	0	110,0	0
		1,5	0	85	0	92,3	0	90,5	0	89,5	0	107,3	0
		0,5	∞	0	75	0	82,5	0	77,7	0	74,9	0	94,5
		1	∞	0	67	0	73,3	0	70,8	0	69,6	0	83,8
		0,5	1	65	65	58,8	58,8	55,7	55,7	53,7	53,7	66,6	66,6

References

[1] Neuber H, Kerbspannungslehre. Theory of notches [Edwards JW, Eng Trans]. Ann Arbor MI: Springer-Verlag; 1946.
[2] Peterson RE. Notch sensitivity. In: Sines G, Waisman JL, editors. Metal fatigue. New York; 1959.
[3] Taylor D. The theory of critical distances: a new perspective in fracture mechanics. Elsevier; 2007.
[4] Navarro A, de los Rios ER. An alternative model of the blocking of dislocations at grain boundaries. Philos Mag A 1988;57:37–42.
[5] Navarro A, de los Rios ER. Short and long fatigue crack growth: a unified model. Philos Mag A 1988;57:12–36.
[6] Chaves V, Navarro A. Application of a microstructural model for predicting notch fatigue limits under mode I loading. Int J Fatigue 2009;31(5):943–51.
[7] Findley WN. A theory for the effect of mean stress on fatigue of metals under combined torsion and axial load or bending. J Eng Ind 1959;81(4):301–6.
[8] Brown MW, Miller KJ. A theory for fatigue under multiaxial stress-strain condition. Proc Inst Mech Eng 1973;187:745–56.
[9] Koutiri I, Bellett D, Morel F. The effect of mean stress and stress biaxiality in high-cycle fatigue. Fatigue Fract Engng Mater Struct 2018;41(2):440–55.
[10] Gough HJ, Pollard HV, Clenshaw WJ. Some experiments on the resistance of metals to fatigue under combined stresses. In: Ministry of supply, aeronautical research council reports and memoranda. London: His Majesty's Stationary Office; 1951. p. 1–141.
[11] Murakami Y. Metal fatigue: effect of small defects and non-metallic inclusions. Elsevier; 2002.
[12] Susmel L, Tayor D. A critical distance/plane method to estimate finite life of notched components. Int J Fatigue 2012;38:7–24.
[13] Susmel L, Taylor D. Two methods for predicting the multiaxial fatigue limit of sharp notches. Fatigue Fract Eng Mater Struct 2003;26:821–33.
[14] Fatemi A, Gates N, Socie DF, Pham N. Fatigue crack growth behaviour of tubular aluminium specimens with a circular hole under axial and torsion loadings. Eng Fract Mech 2014;123:137–47.
[15] Chaves V, Beretta G, Navarro A. Biaxial fatigue limits and crack directions for stainless steel specimens with circular holes. Eng Fract Mech 2017;174:139–54.
[16] Chaves V, Beretta G, Balbin JA, Navarro A. Fatigue life and crack growth direction in 7075–T6 aluminium alloy specimens with a circular hole under biaxial loading. Int J Fatigue 2019;125:222–36.
[17] Susmel L. Multiaxial notch fatigue: from nominal to local stress/strain quantities. Woodhead Publishing; 2009.

[18] Chaves V, Navarro A, Beretta G, Madrigal C. Microstructural model for predicting high cycle fatigue strength in the presence of holes under proportional biaxial loading. Theor Appl Fract Mec 2014;73:27–38.
[19] Carpinteri A, Spagnoli A, Vantadori S, Viappani D. A multiaxial criterion for notch high cycle fatigue using a critical-point method. Eng Fract Mech 2008;75:1864–74.
[20] El Haddad MH, Topper TH, Smith KN. Prediction of non propagating cracks. Eng Fract Mech 1979;11(3):573–84.
[21] Susmel L. A unifying approach to estimate the high-cycle fatigue strength of notched components subjected to both uniaxial and multiaxial cyclic loadings. Fatigue Fract Eng Mater Struct 2004;27(5):391–411.
[22] Taylor D. Notch size effect in multiaxial fatigue. In: Susmel L, Tovo R, editors. Progettazione a fatica in presenza di multiassialitá tensionali. Ferrara; 2005.
[23] Chaves V, Navarro A. Fatigue limits for notches of arbitrary profile. Int J Fatigue 2013;48:68–79.
[24] Navarro A, Vallellano C, Chaves V, Madrigal C. A microstructural model for biaxial fatigue conditions. Int J Fatigue 2011;33:1048–54.
[25] Timoshenko S, Goodier JN. Theory of elasticity. McGraw-Hill; 1934.
[26] Vallellano C, Navarro A, Dominguez J. Fatigue crack growth threshold conditions at notches. Part I: Theory. Fatigue Fract Eng Mater Struct 2000;23:113–21.
[27] Gao Y, Ricoeur A. The refined theory of plane problems for one-dimensional quasicrystalline bodies. J Appl Mech 2012;79:011004.
[28] Endo M. Effects of small defects on the fatigue strengths of steel and ductile iron under combined axial/torsional loading. In: Ravichandran KS, Ritchie RO, Murakami Y, editors. Small fatigue cracks: mechanics mechanisms and applications. Elsevier; 1999.
[29] Endo M. The multiaxial fatigue strength of specimens containing small defects. In: Carpinteri A, de Freitas M, Spagnoli A, editors. Biaxial/multiaxial fatigue and fracture ESIS publication. Elsevier; 2003. p. 243–64.
[30] Murakami Y, Endo M. Quantitative evaluation of fatigue strength of metals containing various small defects or cracks. Eng Fract Mech 1983;17(1):1–15.
[31] Navarro A, Vallellano C, de los Rios ER, Xin XJ. Notch sensitivity and size effects by a short crack propagation model. In: Engineering Against Fatigue, Proc Int Conf. Rotterdam: AA Balkema Publishers; 1997, Sheffield, 1999.
[32] Beretta G. PhD Thesis. Fatiga en componentes con concentradores de tension bajo carga biaxial. Universidad de Sevilla (España; 2016.
[33] Navarro A, Chaves V, Balbín JA. Variations on a critical distance theme. Int J Fatigue 2021;152:106453.
[34] Morgan D, Quinlan S, Taylor D. Using the theory of critical distances to predict notch effects in fibre composites. Theor Appl Fract Mec 2022;118:103285.